Remote Sensing of Environment 294 (2023) 113630

Contents lists available at ScienceDirect

Remote Sensing of Environment

journal homepage: www.elsevier.com/locate/rse

Development of a methodology for evaluating spaceborne W-band Doppler radar by combined use of Micro Rain Radar and a disdrometer in Antarctica

Alessandro Bracci [a,b], Kaori Sato [c,*], Luca Baldini [a], Federico Porcù [b], Hajime Okamoto [c]

[a] Institute of Atmospheric Sciences and Climate (ISAC), CNR, Rome, Italy
[b] Department of Physics and Astronomy "Augusto Righi", Alma Mater Studiorum University of Bologna, Bologna, Italy
[c] Research Institute for Applied Mechanics, Kyushu University, 6-1 Kasuga-Koen, Kasuga, 816-8580 Fukuoka, Japan

ARTICLE INFO

Keywords:
Remote sensing
Snowfall
Antarctica
MRR
Radar
Disdrometer
Satellite validation
CloudSat
EarthCare
K2W

ABSTRACT

Ground-based snowfall observations over Antarctica are rare due to the harsh environment and high logistical, equipment maintenance, and operational costs. Satellite measurements are crucial to provide continent-wide precipitation estimates, and this highlights the importance of validating the satellite estimates with measurements collected by ground-based Antarctic stations. The NASA CloudSat satellite, launched in 2006, is equipped with a 94 GHz (W-band) Cloud Profiling Radar (CPR) that provides measurements of reflectivity profiles of clouds and precipitation, whereas the incoming ESA/JAXA EarthCARE mission will add Doppler capability to a 94 GHz radar. This study explores how the synergy between two instruments available at most Antarctic stations, i.e., Micro Rain Radar (24 GHz, K-band) and laser disdrometer, can be used to validate satellite-borne W-band radar measurements, including Doppler estimates. A new validation methodology (K2W) was proposed to combine these instruments for simulating the 94 GHz reflectivity and Doppler measurements from Micro Rain Radar spectra. Assessment of the proposed K2W conversion methodology showed that the CloudSat Z_e profiles can be simulated by the method with 0.2 dB mean difference at the lowest satellite radar range bin when time lag within ±12.5 min and the distance within 25 km around the CloudSat overpass were considered. With the K2W method, the 94 GHz Doppler velocity below 1 km altitude that would be observed by EarthCARE was obtained, and the standard deviation of the simulated Doppler velocity was found to be smaller than about 0.2 m s^{-1}. The simulated 94 GHz Doppler radar profile information, which is less affected by attenuation compared to ground-based 94 GHz radar, will significantly improve the quantification of precipitation over Antarctica. This methodology will be applied to further assess the EarthCARE CPR Doppler velocity measurement accuracy as well as the Level 2 standard products for precipitation in Antarctica and at many other ground observation sites.

1. Introduction

Precipitation in Antarctica influences the Earth's hydrological cycle and energy budget and can reveal significant effects of climate change. Antarctic precipitation usually occurs in the form of solid precipitation, which is the most important positive term of the surface mass balance of the Antarctic Ice Sheet, which in turn influences global climate variability and sea level rise (Frezzotti et al., 2013). Recent increases in the loss of mass ice are likely related to the warming of the ocean, but precipitation can influence this trend; that is, increases in precipitation related to climate change could compensate for the contribution of the ice sheet to sea level rise (Medley and Thomas, 2019). The Coupled Model Intercomparison Project Phase 6 (CMIP6) General Circulation Models (GCMs) suggests an increase in the amount of precipitation over Antarctica under all considered emissions scenarios, but with relatively large temperature and precipitation projection ranges (the Intergovernmental Panel on Climate Change (IPCC), Sixth Assessment Report (AR6) (IPCC, 2021)). The IPCC AR6 reported that majority of the CMIP phase 5 (CMIP5) models overestimates current Antarctic precipitation and little improvement have been observed in the representation of Antarctic precipitation in the CMIP6 models. Unfortunately, precipitation measurements collected at the surface are extremely scarce. There are no data for most of the continent, and the major sources of information about precipitation are satellite estimates or reanalysis models.

* Corresponding author.
E-mail addresses: a.bracci@isac.cnr.it (A. Bracci), sato@riam.kyushu-u.ac.jp (K. Sato), l.baldini@isac.cnr.it (L. Baldini), federico.porcu@unibo.it (F. Porcù), okamoto@riam.kyushu-u.ac.jp (H. Okamoto).

https://doi.org/10.1016/j.rse.2023.113630
Received 27 December 2022; Received in revised form 10 May 2023; Accepted 15 May 2023
Available online 25 May 2023

This reinforces the urgency to correctly quantify precipitation and distinguish its phase at small spatial scales.

The National Aeronautics and Space Administration (NASA) CloudSat 94 GHz Cloud Profiling Radar (CPR) has been the reference for obtaining precipitation estimates and validating models since 2006 because of its ability to profile the structure of clouds from space. In 2024, the mission EarthCARE (EC), by the European Space Agency (ESA) and Japan Aerospace Exploration Agency (JAXA), will put a Cloud Profiling Radar (EC-CPR) in orbit with increased sensitivity with respect to the CloudSat instrument and that will allow Doppler profiling for the first time (Illingworth et al., 2015). All of the satellite and reanalysis products require extensive validation in Antarctica, both to verify assumptions underlying retrievals and to quantify uncertainties.

Ground-based validation of satellite products is not trivial because of differences in sampling areas, blind zones close to the ground where satellite measurements are unreliable, and the rarity of overpasses with precipitation. CloudSat validation has been performed in several ways, mostly relying on ground-based radars operating at different frequencies, not necessarily that of CPR (Protat et al., 2009). The use of a longer radar wavelength has the advantage of being less affected by attenuation from hydrometeors. The disdrometer (usually laser) and Micro Rain Radar (hereinafter MRR), a 24 GHz Doppler radar profiler manufactured by METEK GmbH, Germany, are relatively common precipitation instruments available at stations in Antarctica. These instruments are suitable for unattended operation in the Antarctic environment. Recent studies in Antarctica (Bracci et al., 2021) and in the Arctic (Schoger et al., 2021) have demonstrated that the synergy of these instruments provides reliable information on precipitation levels and microphysics. At 24 GHz, the attenuation effects due to propagation through snow are considered negligible (Maahn and Kollias, 2012), contrary to the case with propagation through rain. Therefore, validation of CloudSat and EarthCARE must take into account such instruments, particularly for Antarctica, although other aspects, such as differences in frequency, sensitivity, co-location and instrument sampling between ground-based and satellite-borne radar, among other issues, should be taken into consideration.

In this study, we developed a method to obtain the 94 GHz (W-band) radar reflectivity and Doppler profiles from radar Doppler spectrum at 24 GHz (K-band) and disdrometer observations on the ground. Our approach allows comparison and validation of radar reflectivity and Doppler profiles between ground-based and satellite-borne radar using affordable and low-maintenance instrumentation at the surface. This instrumentation can also be deployed in harsh and extreme regions, such as Antarctica, thus increasing the number of validation sites. Furthermore, obtaining Doppler profiles could be beneficial for validating measurements from the next ESA/JAXA EarthCARE satellite mission.

The remainder of this manuscript is organized as follows. Section 2 describes the Mario Zucchelli Station (MZS) site, instrumentation, and the datasets used. Data processing and all methodologies are also described. Section 3 compares data and discusses the consistency between radar and disdrometer observations in terms of radar reflectivity and particle velocities. Finally, Section 4 presents our conclusions, underlining the primary outcomes and the potential of the proposed method for future work.

2. Instruments and dataset

2.1. MZS Antarctic observatory

MZS (74.7°S, 164.1°E, 10 m a.s.l.) is located at Terra Nova Bay along the Ross Sea coast of Northern Victoria Land, Antarctica. It lies close to the Transantarctic Mountains, which to some extent protect the site against the strong katabatic winds originating over the Antarctic Plateau. However, large low-pressure systems persisting over the Ross Sea and approaching the coast give rise to the so-called barrier wind that often affects MZS during precipitation events. In the framework of the project "Antarctic Precipitation Properties" (APP) of the Italian National Antarctic Research Program (PNRA), a Micro Rain Radar (specifically an MRR2 model) and a Parsivel disdrometer manufactured by OTT HydroMet GmbH, Germany, have been installed since December 2016 to investigate, monitor, and quantify precipitation events at MZS. The collocated instrumentation lies on the rooftop of a container 6 m above ground level on the outskirts of the station area. Although MZS is open only during the austral summer, unattended power supply facilities allow data collection all year round.

2.2. Micro Rain Radar

The MRR is a vertical pointing Doppler profiler (Peters et al., 2002), which is well suited for installation in harsh environments and difficult-to-access regions for long-term unattended observations due to its compact design, low energy consumption, and low maintenance requirements as well as affordable cost. Data acquired by the MRR2 used in this work operates at 24 GHz (K-band), collecting Doppler power spectra in 64 bins along 32 vertical range bins. In contrast to the most common setting for vertical resolution (100 m), which is used at other MRR installations in Antarctica (Grazioli et al., 2017a; Scarchilli et al., 2020; Souverijns et al., 2017), the MRR2 at MZS has been set to a vertical resolution of 35 m, which makes it possible to obtain the first trustworthy measurement 105 m above the surface. This is particularly helpful for comparative analysis with other ground-based instruments (i.e., disdrometers or pluviometers; see Bracci et al., 2021) and especially in continental Antarctica, where the influence of low-level katabatic wind during precipitation can lead to sublimation of snowfall in the lower atmospheric layers before reaching the ground (Bracci et al., 2022; Grazioli et al., 2017b). MRR2 Doppler spectra at 1-min time resolution were used in this study. To analyze their consistency with Parsivel data, the measurements collected at 105 m were considered, while complete vertical profiles (from 105 to 1050 m) were taken into account in comparison with CloudSat overpasses occurred on 4 December 2018 in which 272 satellite profiles were used.

2.3. Parsivel disdrometer

The Parsivel optical laser-based disdrometer (hereafter Parsivel) deployed at MZS provides particle size and its velocity. It detects microphysical features of hydrometeors passing through the horizontal laser matrix, simultaneously measuring the diameter and velocity of falling particles sorted in a 32×32 dimension/speed matrix (Löffler-Mang and Joss, 2000). The disdrometer sensor consists of two heads (one transmitter, one receiver), with a laser beam continuously emitted by the transmitter toward the receiver. As hydrometeors cross the beam, they produce a decrease in the received voltage. The diameter and speed of the particles can be inferred from the amount and duration of the voltage drop. Similar to MRR, Parsivel disdrometers are largely employed in complex and severe environments due to their usability, sturdiness, and reliability. The count matrix of falling particles at 1 min time steps was considered.

2.4. Spaceborne cloud radar

The NASA CloudSat mission was launched into the Afternoon Constellation (A-Train) sun-synchronous orbit with mean equatorial altitude of 705 km in 2006 carrying a CPR (Tanelli et al., 2008). The CloudSat CPR is a 94 GHz (W-band) nadir-pointing radar, which measures the radar reflectivity factor of clouds and precipitation with a detection sensitivity of about −30 dBZ, at approximately 240 m vertical oversampling and 1.4 km/1.7 km cross-track/along-track resolution (Tanelli et al., 2008). The CPR is currently the most sensitive instrument capable of detecting the wide range of the precipitation size spectrum (Stephens et al., 2018). In 2018, CloudSat exited the A-Train and has been operating in the C-Train orbit since May 2018, which is 16.5 km

lower than the A-Train in Daytime-Only Operations (DO-Op) mode. The ESA and JAXA joint mission EarthCARE is scheduled for April 2024 and will carry a 94 GHz Doppler Cloud Profiling Radar (EC-CPR). The EC-CPR will fly at ~400 km orbit, collecting vertical motions of clouds and precipitation in addition to Z_e at vertical/horizontal resolution of 100 m/500 m, with a minimum detectable reflectivity of −36 dBZ (Hagihara et al., 2022). The latest global simulation of EC-CPR Doppler velocity measurements with a Global Cloud System Resolving Model and a satellite data simulator revealed that the differences between the simulated observation and the true velocity for precipitation was <0.5 m s^{-1} at $Z_e > 0$ dBZ for the low pulse repetition frequency (PRF) case and would be smaller for the high PRF case planned for EarthCARE (Hagihara et al., 2022).

2.5. Data processing

2.5.1. MRR2 data

The MRR2 was originally designed to detect rainfall, exploiting the relationship between the velocity and dimension of falling raindrops. When MRR2 is employed to measure snow, specific procedures must be applied to improve the sensitivity, remove artifacts like the aliasing effects on Doppler spectra, in order to obtain dependable snow observations. Consequently, the post-processing algorithm for raw MRR2 data based on Maahn and Kollias (2012) is applied to improve MRR2 snow measurements.

2.5.2. Parsivel data

Laser disdrometers are widely used to detect the distribution of liquid hydrometeor size, and recently have also been used to determine the particle size distribution (PSD) of solid hydrometeors despite some well-known limitations (Battaglia et al., 2010). In this respect, disdrometers are particularly prone to artifacts when there is strong horizontal wind, as the detection of hydrometeors assumes that particles pass across the measurement area with a vertical trajectory rather than in a slanted path, as would be in the case of strong wind. Such shortcomings are particularly significant when studying snowfall due to the smaller fall velocity of snow particles than that of rain. Several approaches have been proposed to avoid or at least to reduce the influence of wind on disdrometer measurements, including setting a wind speed threshold to optimize reliability (Capozzi et al., 2020; Molthan et al., 2016; Souverijns et al., 2017), comparing disdrometer data with other instruments to mitigate any adverse effects (Bracci et al., 2021), and using a filter for artifacts based on reported relationships for raindrop falling velocity (Scarchilli et al., 2020).

In this work, the last approach is used. From raw disdrometer data of the 2019–2020 Antarctic summer season, snow particles with a falling velocity > 50% increased value (Chen et al., 2016; Scarchilli et al., 2020) of the velocity-diameter relation of raindrops by Atlas et al. (1973) (eventually corrected for the height of measurements with a multiplicative factor $F(h)$ as in Foote and Du Toit, 1969) were excluded. In particular, excluded are particles for which the velocity and diameter relation satisfied Eq. (1),

$$\mathrm{V}(D) > (1+\mathrm{th}) \times (9.65 + 10.3exp(-0.6D) \times F(\mathrm{h})) \quad (1)$$

where D (in mm) and V (in m s^{-1}) are the diameter and fall velocity measured by the disdrometer, and th is a value of 0.5 taken from the mentioned references. Because of the strong wind observed at the ground (>15 m s^{-1}) during the precipitation event (3–4 December 2018) in which the CloudSat overpass occurred, for such case we used a stricter velocity mask, removing particles with a falling velocity greater than the velocity by Atlas et al. (1973), i.e., using Eq. (1) with $th = 0$. It is worth noting that the use of the criterion described by Eq. (1), based on a relation for raindrops instead of for snow, provides a conservative threshold for eliminating biased data and aims to preserve raw data as much as possible. Then the filtered count matrix of falling hydrometeors detected by the disdrometer at observation time $t_k = k\Delta t$ ($k = 1,2, \ldots$), where Δt is the temporal observation interval, was used to obtain the particle size distribution (PSD) of snowfall as

$$\mathrm{N}(D_i, t_k) = \sum_{j=1}^{j_{max}} \frac{n_{i,j}(t_k)}{A\Delta t\, v_j \Delta D_i}; i = 1, \ldots\ldots, i_{max} \quad (2)$$

$\mathrm{N}(D_i,t_k)$ has the unit of m^{-3} mm^{-1}, A is the Parsivel detection area, subscript i is the index of the diameter bins D_i of width ΔD_i, while j is the index of the velocity bins v_j of width Δv_j, $i_{max} = 32$ and $j_{max} = 32$. $n_{i,j}(t_k)$ is the sum of $n'_{i,j}(t)$, which is the number concentration for the i-th size bin and j-th velocity bin obtained at time t, between $t = t_k - \Delta t/2$ and $t_k + \Delta t/2$ described by,

$$n_{i,j}(t_k) = \int_{t_k-\Delta t/2}^{t_k+\Delta t/2} n'_{i,j}(t)\, dt \quad (3)$$

Δt is set to 1 min in order to collect a sufficient number of hydrometeors for each class and obtain meaningful PSD estimates. Note that in Eq. (2), $n_{i,j}(t_k)$ is set to 0 for the i, j-th bins where Eq. (1) is satisfied.

2.5.3. CloudSat profiles

For the satellite data, we used the 94 GHz CloudSat 2B-GEOPROF (release P1 R05) radar reflectivity factor data. For the cloud/hydrometeor mask, the CloudSat-only cloud mask scheme (C1 mask) of Hagihara et al. (2010), which was originally developed and tested with shipborne 94GHz cloud radar observations in mid-latitude in Western Pacific ocean (Okamoto et al., 2007) and in Tropical Western Pacific Ocean (Okamoto et al., 2008), was used. It utilizes the CPR level 2B-GEOPROF (R05) hydrometeor mask value and a spatial continuity test. It assigns a confidence level of significance for the signal from noise with values ranging from 0 to 40 (Marchand et al., 2008). In the C1 mask, a hydrometeor mask value ≥ 20 (i.e., range bins where the backscattered power is greater than the mean noise power plus one standard deviation) was adopted, which can detect small-scale water clouds at lower altitudes (Hagihara et al., 2010). The C1 cloud-masked data is provided as the CloudSat-CALIPSO Merged Dataset by JAXA. Radar range bins near the surface that were significantly affected by surface clutter with the surface clutter identification algorithm in R05 (Marchand and Mace, 2018) were assigned a CloudSat hydrometeor mask value of 5 and were excluded from our analysis. The CloudSat Z_e profiles after hydrometeor/surface clutter masking and correction for gaseous attenuation were further matched to the vertical resolution of MRR2. A typical precipitation event over MZS observed by CloudSat on 4 December 2018, was analyzed. The lowest radar range bins that we compared to MRR2 had a confidence level of 40, which indicates a high probability of a strong echo from hydrometeors (Marchand and Mace, 2018).

2.6. K2W: methodology for spaceborne W-band radar validation

This Section discusses the validation methodology proposed that combines MRR2 and disdrometer data and scattering simulations.

2.6.1. Simulation of radar reflectivity factor and Doppler velocity at the K-band from disdrometer measurements

The Z_e and Doppler velocity V_D in the absence of vertical motions at K-band at range (height) gate index R and time t_k are given by the following definitions:

$$Z_{e,K}(R,t_k) = 10^{18}\frac{\lambda^4}{\pi^5|\mathrm{K_w}|^2}\int_{\mathrm{D_{min}}}^{\mathrm{D_{max}}} C_{\mathrm{bk,K}}(R,D,t_k)\,\mathrm{N}(R,D,t_k)\,\mathrm{d}D\ \left(\mathrm{mm^6 m^{-3}}\right) \quad (4)$$

$$V_{D,K}(R,t_k) = \frac{\int_{\mathrm{D_{min}}}^{\mathrm{D_{max}}} \mathrm{N}(R,D,t_k)\, C_{\mathrm{bk,K}}(R,D,t_k)\, v_t(R,D,t_k)\,\mathrm{d}D}{\int_{\mathrm{D_{min}}}^{\mathrm{D_{max}}} \mathrm{N}(R,D,t_k)\, C_{\mathrm{bk,K}}(R,D,t_k)\,\mathrm{d}D}\ \left(\mathrm{m\ s^{-1}}\right) \quad (5)$$

λ (m) is the wavelength at K-band (12.49 mm), the $|\mathrm{K_w}|^2$ value is

related to the dielectric constant of liquid water at the wavelength of interest (Bringi and Chandrasekar, 2001), and the value of the constant for MRR2 is set to 0.92 (Souverijns et al., 2017), while it is set to 0.75 for the case of CloudSat W-band radar (Tanelli et al., 2008). $C_{bk,K}(R,D,t_k)$ (m^2) and $v_t(R,D,t_k)$ are the K-band backscattering cross-sections and terminal velocity of a particle of diameter D, respectively, and $N(R,D,t_k)$ is the particle size distribution with D varying between a minimum particle size D_{min} and maximum particle size D_{max}. Note that Eq. (4) is a general expression of Z_e and does not require any approximations about scattering regimes.

The Z_e at time t_k and for the K-band MRR frequency estimated from disdrometer measurements, $Z_{e,disd}(t_k)$, is given by

$$Z_{e,disd}(t_k) = 10^{18}\frac{\lambda^4}{\pi^5|K_w|^2}\sum_{i=1}^{i_{max}} C_{bk,K}(D_i)N(D_i,t_k)\,\Delta D_i \ \left(\mathrm{mm^6 m^{-3}}\right) \tag{6}$$

It is noted that, $C_{bk,K}$ depends on particle habit and diameter, and once the habit is specified at each t_k the dependence of $C_{bk,K}$ on habit can be omitted. Therefore, the t_k dependence of $C_{bk,K}$ is omitted in Eq. (6). The disdrometer-derived Doppler velocity $v_c(t_k)$ at the K-band in the absence of vertical motions is given by the following formula (Adirosi et al., 2016):

$$v_c(t_k) = \frac{\sum_{i=1}^{i_{max}} N(D_i,t_k)C_{bk,K}(D_i)\,v_t(D_i,t_k)\,\Delta D_i}{\sum_{i=1}^{i_{max}} N(D_i,t_k)C_{bk,K}(D_i)\,\Delta D_i} \ \left(\mathrm{m\ s^{-1}}\right) \tag{7}$$

Where $v_t(D_i,t_k)$ is the number concentration weighted mean terminal velocity of the particles in the i-th size bin derived from Parsivel raw data for the period of Δt at t_k, and it is given by,

$$v_t(D_i,t_k) = \frac{\sum_{j=1}^{j_{max}} n_{i,j}(t_k)v_j\Delta v_j}{\sum_{j=1}^{j_{max}} n_{i,j}(t_k)\Delta v_j} \ \left(\mathrm{m\ s^{-1}}\right). \tag{8}$$

For the convenience of the discussions in the later sections, moving averages of $N(D_i,t_k)$, $v_c(t_k)$ and $v_t(D_i,t_k)$ are introduced, where these values (i.e., $\overline{N_M}(D_i,t_k)$, $\overline{v_{c,M}}(t_k)$, $\overline{v_{t,M}}(D_i,t_k)$) are time averaged for $M\Delta t$ minutes, from $t_k - M\Delta t/2$ and $t_k + M\Delta t/2$, and reported at every t_k as:

$$\overline{N_M}(D_i,t_k) = \begin{cases} \frac{1}{M}\sum_{k'=k-(M-1)/2}^{k+(M-1)/2} N(D_i,t_{k'}) \ \text{(when M is odd)} \\ \frac{1}{M}\left[\sum_{k'=k-M/2+1}^{k+M/2-1} N(D_i,t_{k'}) + 0.5N\left(D_i,t_{k-M/2}\right) + 0.5N\left(D_i,t_{k+M/2}\right)\right] \ \text{(when M is even)} \end{cases}. \tag{9}$$

Here, $t_{k'} = k'\,\Delta t$. Substituting Eq. (2) into Eq. (9) gives

$$\overline{N_M}(D_i,t_k) = \sum_{j=1}^{j_{max}} \frac{n_{i,j,M}(t_k)}{A\ (M\Delta t)\ v_j\Delta D_i}, \tag{10}$$

where $n_{i,j,M}(t_k)$ is the cumulative concentration of $n_{i,j}(t_k)$ for the period written as,

$$n_{i,j,M}(t_k) = \begin{cases} \sum_{k'=k-(M-1)/2}^{k+(M-1)/2} n_{i,j}(t_{k'}) \ \text{(when M is odd)} \\ \sum_{k'=k-M/2+1}^{k+M/2-1} n_{i,j}(t_{k'}) + 0.5n_{i,j}\left(t_{k-M/2}\right) + 0.5n_{i,j}\left(t_{k+M/2}\right) \ \text{(when M is even)} \end{cases}. \tag{11}$$

The corresponding time averaged value of $v_c(t_k)$ can then be written as,

$$\overline{v_{c,M}}(t_k) = \frac{\sum_{i=1}^{i_{max}} \overline{N_M}(D_i,t_k)\,C_{bk,K}(D_i)\,\overline{v_{t,M}}(D_i,t_k)\,\Delta D_i}{\sum_{i=1}^{i_{max}} \overline{N_M}(D_i,t_k)\,C_{bk,K}(D_i)\,\Delta D_i}, \tag{12}$$

where,

$$\overline{v_{t,M}}(D_i,t_k) = \frac{\sum_{j=1}^{j_{max}} n_{i,j,M}(t_k)v_j\Delta v_j}{\sum_{j=1}^{j_{max}} n_{i,j,M}(t_k)\Delta v_j}. \tag{13}$$

In this study, $\overline{v_{t,M}}(D_i,t_k)$ in Eq. (13) is approximated by the value of its power law fit in order to establish a monotonically increasing $v_t(D)$ relationship in the following form,

$$\overline{v_{t,M}}(D,t_k) \simeq a_M(t_k)D^{b_M(t_k)}. \tag{14}$$

Eqs. (10), (12), and (13) reduces to Eqs. (2), (7), and (8) for M = 1, respectively. As a result, $\overline{N_M}(D_i,t_k)$, $\overline{v_{c,M}}(t_k)$, $\overline{v_{t,M}}(D_i,t_k)$ are reported at every t_k (i.e., 1 min time resolution).

The $C_{bk,K}$ in Eqs. (6), (7), and (12) are obtained by the discrete dipole approximation (DDA) (Draine, 1988), which is a scattering theory that can be applied to arbitrary shape particles. In this method, a particle is divided into L subvolume elements and each element is replaced by an electric point dipole (Okamoto, 2002). All the interactions between electric dipoles are fully taken into account, and the scattering problem can be numerically solved. Approximations in the DDA are: (i) approximation of the target boundary by L subvolume elements, and (ii) neglecting the higher-order terms than electric dipoles (Okamoto et al., 1995). Validity criteria of the DDA were established for spheres (Draine and Flatau, 1994) and for non-spherical ice particles (Okamoto, 2002). When such criteria are satisfied, DDA provides accurate results for C_{bk}, where the errors are generally within few percent. In this study, C_{bk} are obtained from the scattering database calculated by DDA for various ice particle shapes (Kuo et al., 2016) at the wavelength of W-band and K-band. Bracci et al., 2021 reshaped the particle types of the discrete dipole approximation (DDA) database of Kuo et al. (2016) into pristine and aggregate categories and found that the aggregate category was the dominant particle type at MZS, prevailing in 75% of precipitation events by comparing the measured Z_e at 105 m from MRR2 and estimated Z_e from Parsivel. The dataset used in that work was found to consist of aggregate particles for > 68% of the precipitation time and for > 74% of the days of CloudSat overpass. Therefore, here, we consider this aggregate category (Bracci et al. (2021)) to obtain $C_{bk,K}(D_i)$ for $Z_{e,disd}$

and $\overline{v_{c,M}}$ in Eqs. (6), (7), and (12).

In Section 3, $Z_{e,disd}$ and $\overline{v_{c,M}}$ are compared to the MRR2 equivalent reflectivity and Doppler velocity observations at 105 m a.g.l. to verify that Parsivel PSD and fall velocity information can reproduce the simultaneous MRR2 measurements. This will be exploited for converting the K-band Doppler spectra into W-band Doppler spectra with the synergy method explained in the following.

2.6.2. Simulation of Doppler spectra at W-band using K-band Doppler spectra (K2W)

A method was developed to simulate 94 GHz reflectivity and Doppler measurements from MRR2 spectra using appropriate $C_{bk}(D)$ and velocity-diameter relationship for precipitation with the aid of Parsivel observations.

MRR2 is a CW-FM radar that processes received signals with two FFTs producing a matrix of received power spectra. At each height gate, such spectra can be converted straightforwardly into spectral reflectivity η by using a calibration constant, a transfer function, and accounting for range R (i.e. height). Lowest level data available to users are presented as a matrix

$$\eta(s,R), s = 0, \ldots, 63; R = 1, \ldots, 32 \quad (15)$$

s is the index of the lines of the Doppler spectrum within a Nyquist interval and $\eta(s,R)$ the reflectivity in m^{-1} of particles with Doppler velocity between v_s and $v_s + \Delta v$ of the sample volume at the height corresponding to the index R. Such lines are equally spaced by a frequency shift that corresponds to a Doppler velocity shift of $\Delta v = \Delta f\, \lambda/2$, and Δf the Nyquist frequency interval (inverse of the sweep repetition

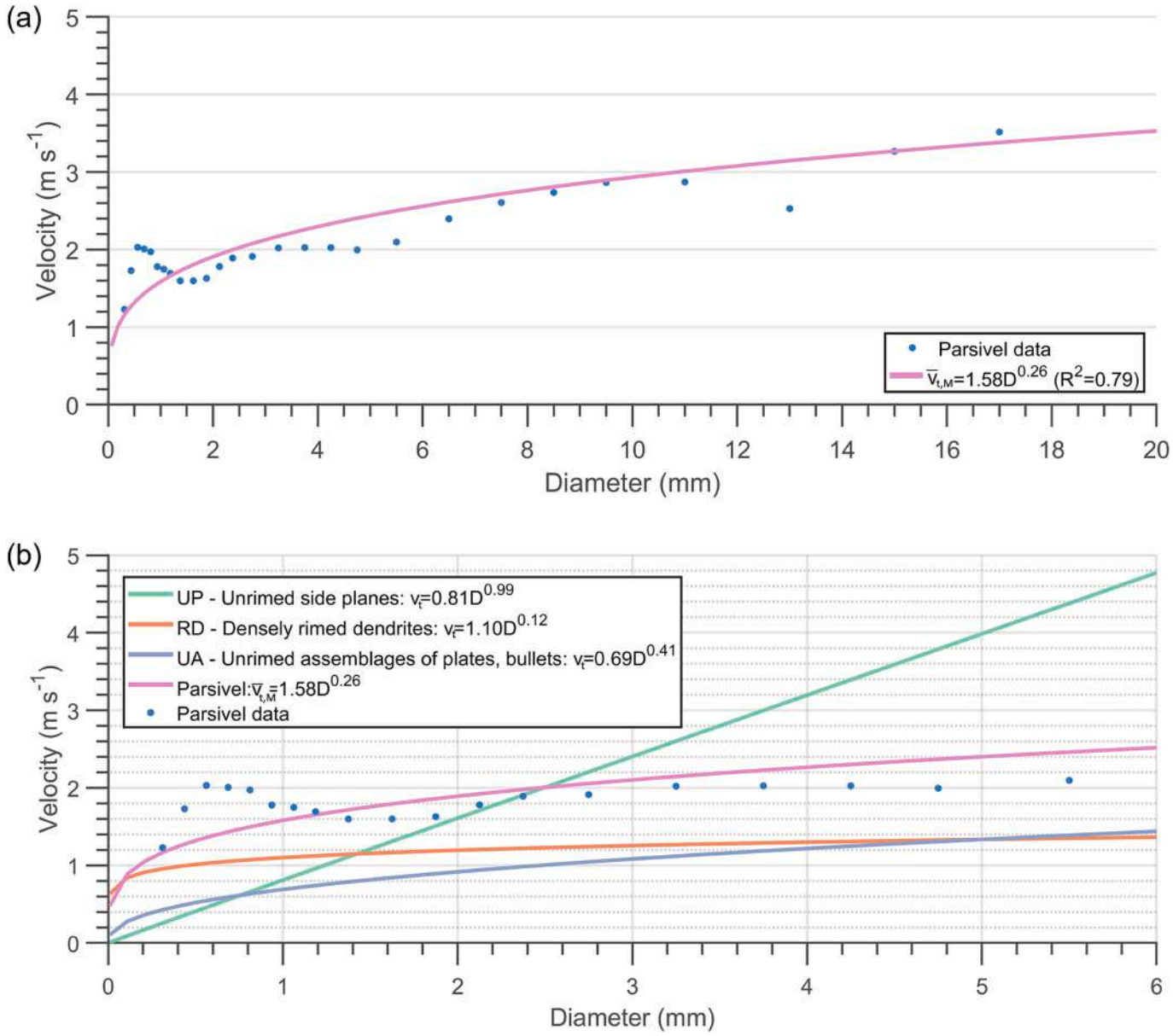

Fig. 1. (a) Example of $\overline{v_{t,M}}(D)$ relationship obtained from Parsivel observations for the precipitation event on 22 November 2019. Dots represent the average velocity for each of the size bins of the disdrometer (Eq. (13)), considering $M\Delta t = 433$ min of Parsivel data. The curve represents the $\overline{v_{t,M}}(D)$ fit calculated using the power-law form (Eq. (14)). The coefficient of determination (R^2) of the fit is reported in the legend. (b) Comparison of the different $v_t(D)$ relationships used in this work for the precipitation event that occurred on 22 November 2019. The curves named UP (Unrimed Planes), RD (Rimed Dendrites), UA (Unrimed Assemblages) refer to the three different $v_t(D)$ relationships from Locatelli and Hobbs (1974) for the different particle habits. The magenta line and dots refer to the power-law fit of the $\overline{v_{t,M}}(D)$ relationship derived from the Parsivel observations and the Parsivel data shown in panel (a), respectively. Note that x-axes range in the two panels are different. (For interpretation of the references to colour in this figure legend, the reader is referred to the web version of this article.)

time) divided by 64. Δv is found to be 0.189 m s^{-1} so that the spectrum is presented in the range from 0 to a Nyquist velocity of v_{Ny} ~12.01 m s^{-1}, which seems adequate in the absence of vertical winds. A spectral reflectivity density with respect to Doppler velocity is obtained as

$$\eta_v(v_s, R) = \frac{\eta(s,R)}{\Delta v} \ \left(\mathrm{m}^{-2}\ \mathrm{s}\right); v_s = s\Delta v\ \left(\mathrm{m\ s}^{-1}\right) \tag{16}$$

For simplicity of notation, we neglect the dependency from the height, eliminating the index R. To obtain the particle size distribution, we express the spectral reflectivity density with respect to particle diameter (in mm) $\eta_D(D)$ (m^{-1} mm^{-1}) through

$$\eta_v(v)\partial v = \eta_D(D)\ \partial D\ \left(\mathrm{m}^{-1}\right). \tag{17}$$

The particle size distribution is then obtained as

$$N(D) = \eta_{\mathrm{D}}(D)/C_{\mathrm{bk}}(D)\ \left(\mathrm{mm}^{-1}\mathrm{m}^{-3}\right), \tag{18}$$

being $C_{bk}(D)$ (m^2) the backscattering cross-section. This part has basically described the PSD retrieval method that can be found in MRR Physical Basics (METEK, 2015). We can repeat the process backward to obtain the reflectivity spectrum at W-band. Let's make explicit the frequency dependency by adding subscripts K and W (K-band and W-band, respectively) where needed. Eq. (18) can be rewritten as

$$N(D) = \eta_{D,K}(D)/\mathrm{C}_{bk,\mathrm{K}}(\mathrm{D})\ \left(\mathrm{mm}^{-1}\mathrm{m}^{-3}\right). \tag{19}$$

If $C_{bk,\mathrm{W}}(D)$ are available in addition to $C_{bk,\mathrm{K}}(D)$ for the same habit of particles, we can obtain

$$\eta_{D,W}(D) = N(D)C_{\mathrm{bk,W}}(D)\ \ \left(\mathrm{m}^{-1}\mathrm{mm}^{-1}\right). \tag{20}$$

Using Eq. (17) the spectral reflectivity density with respect to particle's velocity at W band can be obtained as

$$\eta_{v,W}(v) = \eta_{v,K}(v)\frac{\partial v}{\partial D}\ \frac{C_{\mathrm{bk,W}}(D)}{C_{\mathrm{bk,K}}(D)}\ \frac{\partial D}{\partial v}\ \left(\mathrm{m}^{-2}\ \mathrm{s}\right) \tag{21}$$

Being v=g(D) independent on wavelength, the following relation can be obtained

$$\eta_{v,\mathrm{W}}(v) = \eta_{v,K}(v)\ \frac{C_{bk,\mathrm{W}}(v=\mathrm{g}(D))}{C_{bk,K}(v=\mathrm{g}(D))}\ \left(\mathrm{m}^{-2}\ \mathrm{s}\right). \tag{22}$$

Although the development was conducted assuming a continuous variable v, spectrum is available at the lines v_s. In the development of the method, we made several assumptions. First, the vertical wind was neglected at the ground and therefore, $v = v_t$. Then for the continuous relation $v_t = \mathrm{g}(D)$, we used the $\overline{v_{t,M}}(D, t_k)$ relationship derived from Eq. (14). The sufficient averaging time MΔt required to obtain reliable $\overline{v_{t,M}}(D, t_k)$ relationship will be discussed in later section. At different heights, there could be both an influence of vertical wind and, in addition, a variation of particles' habit. We assume that within 1 km above the surface influence of vertical wind is negligible and particles' habit does not change. $C_{bk,\mathrm{W}}$ and $C_{bk,\mathrm{K}}$ in Eq. (22) are obtained based on DDA as described in subsection 2.6.1. The Z_e and the mean Doppler velocity at W-band ($V_{D,W}$) can be obtained as follows:

$$Z_{e,W} = 10^{18}\frac{\lambda^4_{(W)}}{\pi^5\left(|K_w|^2\right)_{(W)}}\ \int_0^{v_{Ny}} \eta_{v,W}(v)dv\ \left(\mathrm{mm}^6\ \mathrm{m}^{-3}\right) \tag{23}$$

$$V_{D,W} = \frac{\int_0^{v_{Ny}} v\eta_{v,W}(v)\ dv}{\int_0^{v_{Ny}} \eta_{v,W}(v)\ dv}\ \left(\mathrm{ms}^{-1}\right) \tag{24}$$

Fig. 1a shows an example of the $\overline{v_{t,M}}$(D) relationship obtained from Eq. (14) for a precipitation event on 22 November 2019. The coefficients a and b of the power law in this example were derived using MΔt = 433 min of data obtained for the time period corresponding to the duration of the precipitation event (see also Table 1), and the coefficient of determination R^2 is also shown in the figure to assess the quality of the fit (the value of 0.79 is obtained for the case shown). In this subsection and Section 3, three different $v_t(D)$ relationships from the literature (Locatelli and Hobbs, 1974) are also considered for comparison for the estimation of $Z_{e,W}$ and $V_{D,W}$ in Eq. (23) and Eq. (24), respectively, in order to explore the influence of the relationship choice on the conversion procedure. These literature relationships are tailored for different particle habits (namely (UP): unrimed side planes; (RD) densely rimed dendrites, (UA) unrimed assemblages of plates) and were selected to consider the natural variability of snow particles as much as possible. In Fig. 1b, these $v_t(D)$ relationships are shown with that derived from Parsivel for the same precipitation episode as Fig.1a, which were distinctively different from the derived relationship.

Table 1
Dataset used for MRR2-Parsivel consistency test. The velocity-diameter relationships of the falling particles derived from Parsivel observations for each event are also shown as comparison.

Dataset Antarctic summer 2019–2020			*Velocity diameter relationship* ($\overline{v_{t,M}} = aD^b$)	
# event	*Days*	*Precipitation minutes* ($Z_{e,K}$ > -5dBZ)	*Prefactor a*	*Exponent b*
1	*22 Nov 2019*	*433*	*1.58*	*0.24*
2	*5–6 Dec 2019*	*1428*	*1.41*	*0.09*
3	*8–10 Dec 2019*	*1438*	*1.45*	*0.34*
4	*18–20 Dec 2019*	*2552*	*1.37*	*0.11*
5	*28–29 Dec 2019*	*1370*	*1.09*	*0.03*
6	*12 Jan 2020*	*345*	*1.40*	*0.21*
7	*27 Jan 2020*	*673*	*1.14*	*0.15*
8	*31 Jan 2020*	*643*	*1.08*	*0.15*
9	*1–2 Feb 2020*	*595*	*1.40*	*0.12*
Total	***16 days***	***9477***		

3. Results and discussion

This Section assesses the performance of our approach, focusing first on the consistency between MRR2 observations at 105 m a.g.l. and the forward modeled $Z_{e,disd}$ and $\overline{v_{c,M}}$ from Parsivel data and then on a comparison of the simulated and observed CloudSat Z_e profiles using the proposed K2W conversion methodology. Finally, the simulated result of Doppler velocity profile at W-band is also provided.

3.1. Consistency between observed and simulated MRR2 observations

This work focuses on the observations during the Antarctic summer season from November 2019 to February 2020 to evaluate the MRR2–Parsivel consistency and on data of a precipitation event occurred on 3–4 December 2018, for comparison between K2W and CloudSat measurements in conjunction with the satellite overpass (5:00 UTC on 4 December). In the 2019–2020 dataset, days with at least 60 min of continuous precipitation were selected, resulting in 16 days regrouped in nine precipitation events (see Table 1). In addition, two further criteria were adopted: minutes of MRR2 data with values <−5 dBZ (at the lowest range gate) were discarded, as MRR2 data could be incomplete under this threshold (Maahn and Kollias, 2012; Souverijns et al., 2017); minutes of Parsivel data in which < 10 hydrometeor particles were detected were rejected (Scarchilli et al., 2020). By applying these criteria, the dataset consisted of 9477 min of solid precipitation simultaneously collected by MRR2 and Parsivel at MZS (Table 1).

3.1.1. Equivalent radar reflectivity factor and Doppler velocity

Fig. 2 compares the 9477 min of 2019–2020 snowfall data of $Z_{e,K}$ and $Z_{e,disd}$ as well as $V_{D,K}$ (i.e., first moment of MRR2 Doppler spectra) and $\overline{v_{c,M}}$ derived from Parsivel by Eq. (12). The time resolution for the comparison was set to be 1 min. The root mean square error (RMSE), the normalized standard error (NSE), the normalized bias (NB), the slope (S) of linear regression between observed and predicted data, the Pearson correlation coefficient (CC), and the mean difference (MD) of the scatter

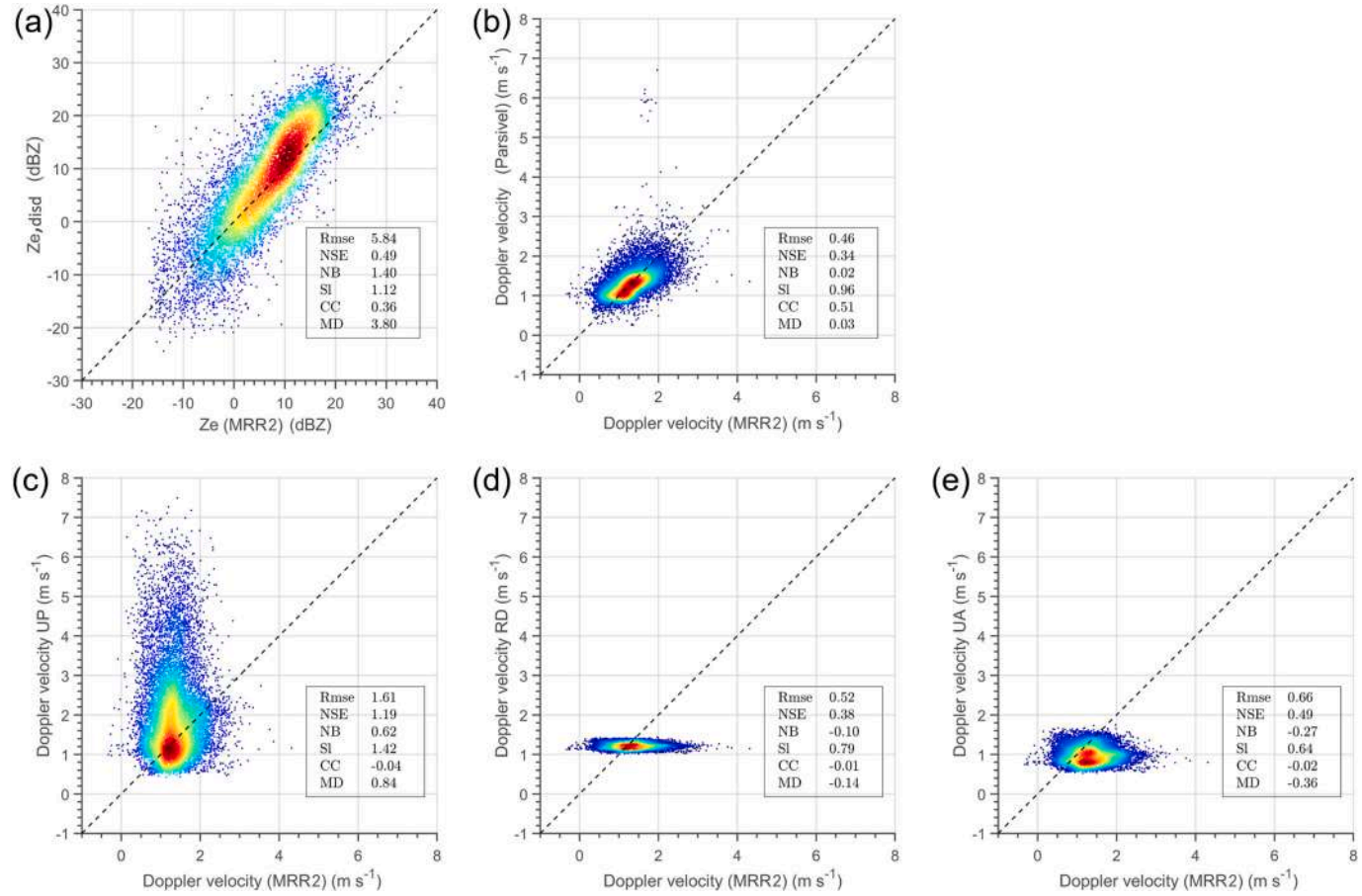

Fig. 2. Density scatter plots for 1-min MRR2 and Parsivel disdrometer data for the 2019–2020 dataset at MZS in terms of (a) $Z_{e,K}$ from MRR2 and $Z_{e,disd}$ calculated from Eq. (6); (b) MRR2 Doppler velocity ($V_{D,K}$) and Parsivel Doppler velocity ($\overline{v_{c,1}}$) obtained using $\overline{v_{t,1}}(D)$ relationship derived from Parsivel measurements; (c) same as (b) but for Parsivel Doppler velocity calculated with $v_t(D)$ relationship from Locatelli and Hobbs, (1974) for Unrimed side Planes (UP); (d) same as (c) but using $v_t(D)$ relationship for densely Rimed Dendrites (RD); (e) same as (c) but using $v_t(D)$ relationship for Unrimed Assemblages (UA). Dots are colored according to the density of data (dark red = high density, dark blue = low density), whereas the dotted line stands for the bisecting line. The values of root mean square error (RMSE), the normalized standard error (NSE), the normalized bias (NB), the slope (S) of linear regression between observed and predicted data, the Pearson correlation coefficient (CC), and the mean difference (MD) are also included in each comparison plot. (For interpretation of the references to colour in this figure legend, the reader is referred to the web version of this article.)

plots are also shown (for a detailed description of the indexes see Gorgucci and Baldini, 2015).

The Parsivel and MRR2 values mostly agreed for the most frequent reflectivity values (around 10 dBZ) using aggregate shape, although positive bias was found for the highest reflectivity values reflecting overestimation of $Z_{e,disd}$ compared to $Z_{e,K}$ (Fig. 2a). The normalized standard error had a value of 0.49, with an MD of 3.8 dBZ.

The Doppler velocity scatter plot depicted in Fig. 2b showed good correspondence between $V_{D,K}$ and $\overline{v_{c,1}}$, where the NSE was around 0.34 with almost no bias. The MD, SI, and CC were considerably better compared to the data shown in Fig. 2c-e, where velocity scatter plots using $v_t(D)$ relationships from the literature in Fig. 1b instead of $\overline{v_{t,1}}(D)$ relationship are shown as a sensitivity test. In Fig.2c-e, the correspondence between the estimated Doppler velocity derived using $v_t(D)$ relationships based on literature and that observed by MRR2 significantly worsened. These results underline the importance of the MRR2-Parsivel pairing, as the relationships in the literature fail to replace the $v_t(D)$ relationship derived from in situ observations.

The Doppler velocities $\overline{v_{c,1}}(t_k)$ obtained by Parsivel (i.e., Eq. (12)) and $V_{D,K}$ from MRR2 at 105 m for the precipitation case observed on 3–4 December 2018 are shown in Fig. 3a, highlighting a general agreement in the trend of velocity but associated with an excessive time variability. The $\overline{v_{c,25}}(t_k)$ obtained by Parsivel agreed better with $V_{D,K}$ values (moving averaged using the same time averaging window of 25 min) correctly following the velocity behavior for the whole precipitation event, except for an anomalous peak at the end of 3 December in Fig.3b. In Fig. 3c, to further see the importance to take into account the variability of $\overline{v_{t,M}}(D)$ relation (Eq. (14)), we replaced the $\overline{v_{t,1}}(D)$ relation used to derive $\overline{v_{c,1}}(t_k)$ in Fig3a with $\overline{v_{t,1740}}(D)$ relation derived with 29 h of Parsivel data collected during the precipitation event, and further used $\overline{N_1}(D_i)$ as in Fig.3a to calculate the Doppler velocity from Eq. (12) shown in blue. The estimated Doppler velocity in Fig.3c led to an overestimation with respect to the $V_{D,K}$ when velocity values were lower and, at the same time, to an underestimation during velocity peaks, resulting in a quite flat time series even using a high time resolution $\overline{N_1}(D_i)$ data. These results suggest that the use of time averaging windows shorter than the duration of the whole precipitation event for $\overline{v_{t,M}}(D)$ calculation allows to take into account the snowflake microphysics that can change on a temporal scale of a few minutes (von Lerber et al., 2017) and that has a significant impact on the falling speed of solid particles (Locatelli and Hobbs, 1974).

The averaging time required for reliable estimation of $\overline{v_{c,M}}$ was explored in Fig. 4. Here, we compared $V_{D,K}$ and $\overline{v_{c,M}}$ both processed in the same way to produce 1 min resolution data as in Fig. 3b for the same data, but with the moving averaging time varying from 1 min to 150 min. The correlation between $V_{D,K}$ at 105 m altitude and $\overline{v_{c,M}}$ decreases when time windows are shorter than about 15 min due to the presence of

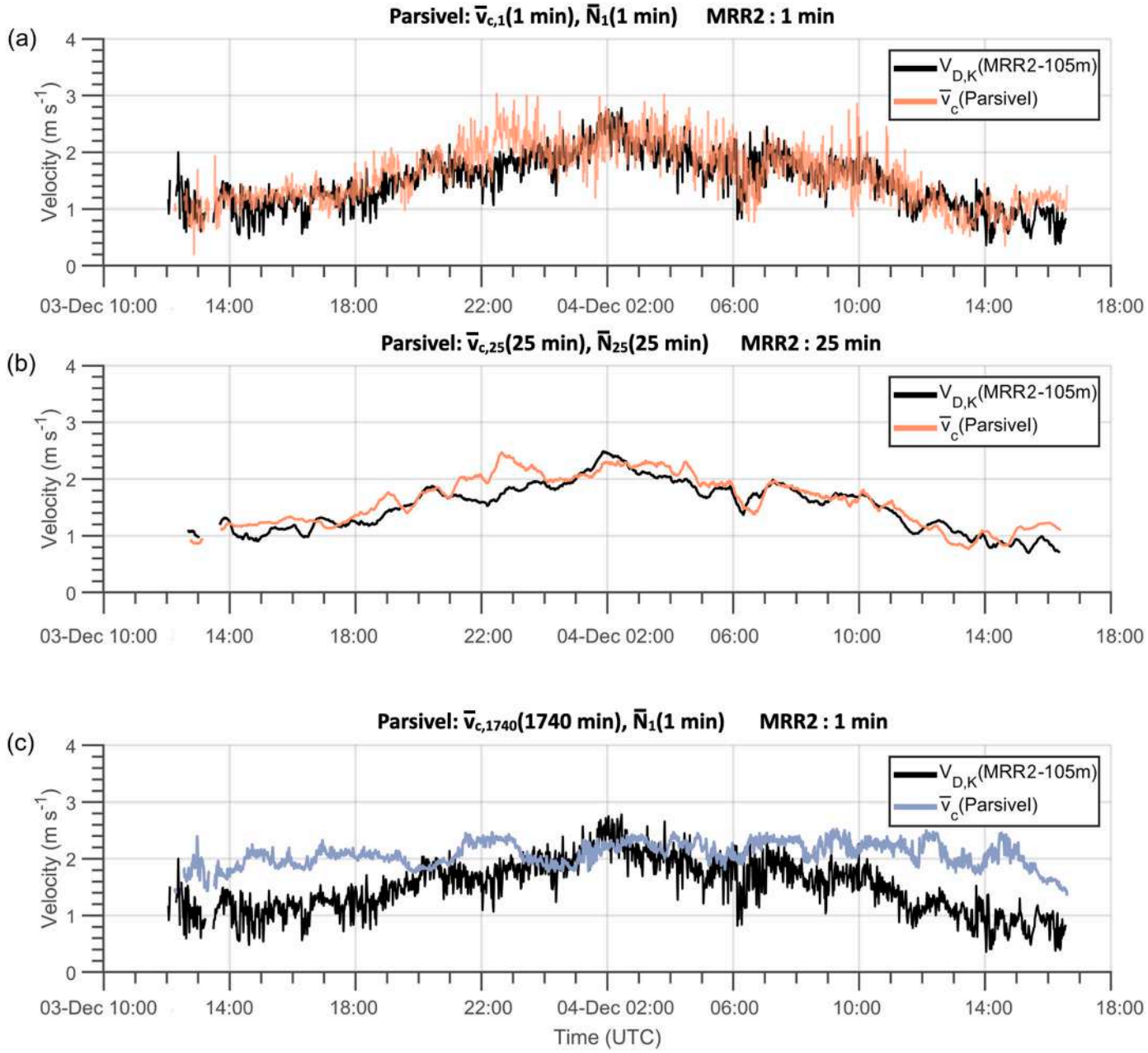

Fig. 3. Time series of Doppler velocity of precipitating particles on 3–4 December 2018. Subplot titles specify the time averaging windows used for processing the Parsivel data to derive $\overline{v_{c,M}}(t_k)$ (i.e., $\overline{v_{t,M}}(D)$ and $\overline{N_M}(D_i)$ in Eq. (12)) and MRR2 data. (a) black line represent MRR2 Doppler velocity $V_{D,K}$ with the original 1-min resolution and orange line indicate the Parsivel derived Doppler velocity $\overline{v_{c,1}}(t_k)$ (Eq. (12)) derived with M = 1. (b) the same as (a) but $V_{D,K}$ (black line) and $\overline{v_{c,25}}(t_k)$ (orange line) obtained with 25 min moving average produced at every 1 min resolution. (c) $V_{D,K}$ plotted with the original 1-min resolution as in (a) and the blue line indicating Parsivel derived Doppler velocity using a $\overline{v_{t,1740}}(D)$ relation derived with 29 h of Parsivel data collected during the precipitation event and $\overline{N_1}(D_i)$. It is apparent that using a unique $\overline{v_{t,1740}}(D)$, the trend of Doppler velocity shown in (a) and (b) completely disappears, even taking into account the $\overline{N_1}(D_i)$ at 1-min resolution, resulting in a nearly flat time series. (For interpretation of the references to colour in this figure legend, the reader is referred to the web version of this article.)

some missing data, measurement errors, and the delay between measurement at the ground and at 105 m height. It was concluded that a minimum time window of ~15 min is required for $\overline{v_{t,M}}(D)$ relationship calculation from Parsivel to ensure that Parsivel and near-ground MRR2 observations statistically sample similar hydrometeors, and this aspect is carefully considered in the following sections.

3.1.2. Simulation of the 94 GHz Doppler spectra

Here we demonstrate the K2W methodology to obtain $Z_{e,W}$ and $V_{D,W}$ profiles from MRR2-Parsivle synergy.

A time series of MRR2 reflectivity profiles at 1 min resolution for the same period of the precipitation event shown in Fig. 3 is presented in Fig. 5a. Heavy snowfall was observed for most of the event, especially during the afternoon of 3 December, with Z_e values higher than 20 dBZ, whereas both heavy and light snow precipitation characterize the minutes around the satellite overpass (5:00 UTC on 4 December). The W-band reflectivity $Z_{e,W}$ at 1 min resolution was obtained from Eq.(23) by the K2W methodology using $\overline{v_{t,15}}(D, t_k)$ relationship (i.e., M = 15 in Eq. (14)) with $\eta_{v,K}(v)$ from MRR2 1 min resolution data without running average in Eq. (22) (Fig. 5b). $Z_{e,W}$ had smaller values than $Z_{e,K}$ as non-

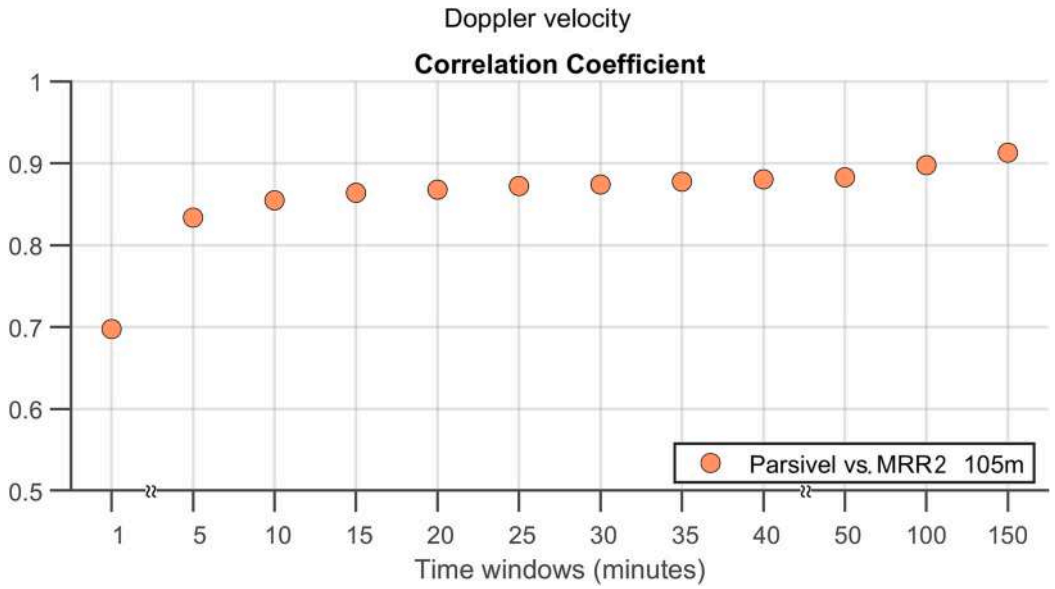

Fig. 4. Correlation coefficients between $V_{D,K}$ at 105 m altitude and $\overline{v_{c,M}}$ derived from Parsivel raw data using different time averaging windows (note x-axis is not to scale).

Rayleigh scattering effects strongly influence the W-band of falling ice/snow hydrometeors, particularly for larger particles (Li and Moisseev, 2020; Liao et al., 2008; Matrosov, 2019, 2021), resulting in a decrease in the W-band reflectivity compared to those at lower frequencies (Matrosov, 2021). Such differences in reflectivity are also known to be effective for determining the microphysical features of solid hydrometeors (e.g., size and shape) in cases where dual-frequency reflectivity measurements are available (Liao et al., 2008).

$Z_{e,W}$ obtained by using the $v_t(D)$ relations for UP, RD and UA are investigated to demonstrate the impact of different $v_t(D)$ relations (Fig. 5c-e). The difference in estimated $Z_{e,W}$ using values from the literature compared to that using Parsivel resulted in a difference larger than 10 dBZ in some radar volumes, and tended to underestimate $Z_{e,W}$ obtained by MRR2-Parsivel synergy. The use of almost linear $v_t(D)$ relationship for UP (Fig. 5c) returned higher $Z_{e,W}$ values compared to those of RD (Fig. 5d) and UA (Fig. 5e), whereas reflectivities found for RD were slightly lower than those in which UA were used. The significant dependence of the converted $Z_{e,W}$ values on the employed $v_t(D)$ relation, which is due to the extreme variability of solid particle microphysics, makes it impossible to simply rely on and use a relationship from the literature for conversion of Doppler spectra in the W-band.

Fig. 6 shows the Doppler velocity profiles estimated by the same procedure for the precipitation event under investigation in the K-band (Fig. 6a) and those simulated for the W-band (Fig. 6b–e), as in Fig.5. The derived $V_{D,W}$ by the K2W method showed similar values with the observed $V_{D,K}$ when the falling velocity was less than about 1.5 m s^{-1}. Above this value, $V_{D,K}$ showed a higher velocity with a difference of about 1 m s^{-1} during the peak. The estimated $V_{D,W}$ using values from the literature resulted in a difference of $>$ 1 m s^{-1} from that derived from K2W method and depended heavily on the $v_t(D)$ relationship used in the conversion procedure. These results stress the importance of having independent, collocated, and simultaneous observations of the falling particles from which the velocity–diameter relationship can be derived, thus underlining the validity of MRR2-Parsivel synergy.

3.2. Comparison of the observed CloudSat and simulated MRR2 profiles in the W-band with K2W

CloudSat overpass over MZS (22.9 km far from MZS as minimum distance) occurred on 4 December 2018, at 05:00 UTC, during snowfall. The simulated and observed W-band reflectivity were investigated in detail.

3.2.1. Temporal variation of reflectivity and Doppler profiles around the overpass

An in-depth analysis of the radar reflectivity (Fig. 7a) and Doppler velocity (Fig. 7b) vertical profiles both in the K-band and W-band shown in Figs. 5 and 6, was performed around the CloudSat overpass time to determine the vertical and time variability of the profiles. The Z_e at K-band maintained similar vertical profiles for about 30 min, i.e., Z_e was higher at the beginning of the time window and increased approaching the ground, then the profile behavior reversed at the end. This pattern was also maintained in the converted W-band profiles, although $Z_{e,W}$ were consistently lower than $Z_{e,K}$. Doppler velocity profiles in the K-band showed enhancement of particle speed toward the surface within the considered time window, with higher values in conjunction with the highest reflectivity near the ground. Use of the predefined $v_t(D)$ relationship for UP and UA overestimated the W-band Doppler velocity simulated with MRR2-Parsivel synergy, while applying the $v_t(D)$ relationship for RD led to an underestimation.

3.2.2. Reflectivity profile comparison

Vertical profiles of W-band reflectivity obtained by K2W around the CloudSat overpass were time averaged for comparison with the horizontally averaged CloudSat Z_e profiles within a certain distance from MZS (Fig. 8).

The lowest measurements of the CloudSat profiles, i.e., at 720 and 960 m a.s.l. were compared to the MRR2 measurements. To properly compare satellite and MRR2 profiles, we computed the mean value of MRR2 reflectivity by equally weighting Z_e for 4 range bins above and 4 range bins below the corresponding CloudSat bin of interest to obtain a similar vertical resolution of 240 m. Following Sections 3.1.1. and 3.2.1, it is expected that relatively short spatial and time averaging (15 min ~ 25 min) would provide a good match in the comparison considering the transition of the cloud system (e.g., Figs. 4 and 7).

As horizontal wind speed at the ground during the overpass was around 15 m s^{-1} (~1 km min^{-1}), we considered this a first approximation of the moving speed of the precipitating system to estimate the one-to-one correspondence between the time and spatial averaging scales. Fig. 9a shows the comparison between the average CloudSat Z_e profile for an area of 25 km around MZS (red) and the corresponding mean $Z_{e,W}$ profile obtained with 25-min time averaging of the 1 min

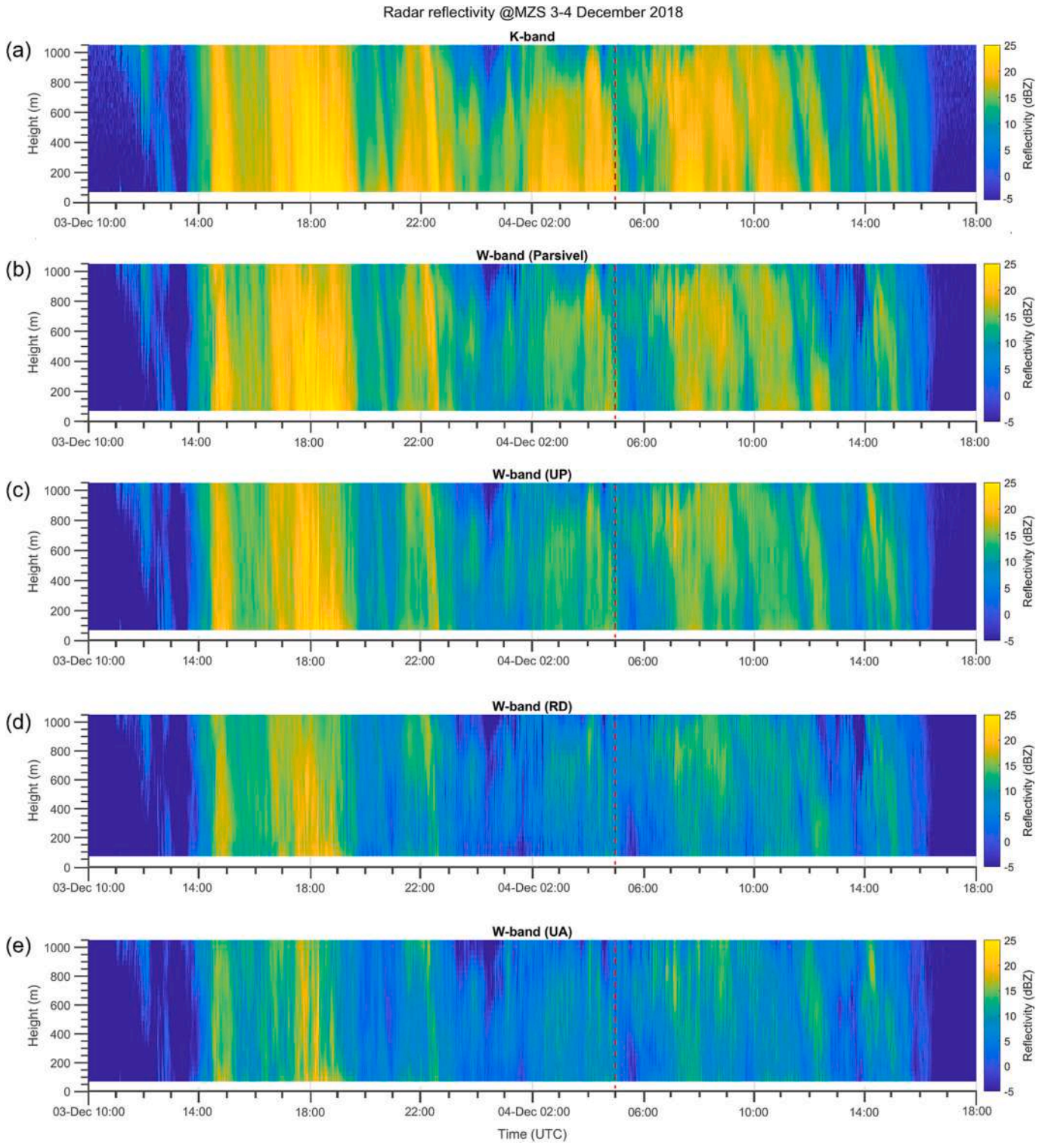

Fig. 5. Time series of the vertical reflectivity profiles at 1-min resolution of the snowfall event on 3–4 December 2018. (a) The K-band reflectivity; (b) W-band reflectivity obtained by the K2W methodology using the $\overline{v_{t,15}}(D, t_k)$ relationships from Parsivel observation; (c), (d), and (e) same as (b) but using $v_t(D)$ relationships for UP, RD and UA taken from Locatelli and Hobbs (1974). Red dotted lines show the time of CloudSat overpass (5:00 UTC on 4 December). (For interpretation of the references to colour in this figure legend, the reader is referred to the web version of this article.)

resolution profiles (time lag of ±12.5 min relative to the CloudSat overpass) obtained by the K2W method using $\overline{v_{t,25}}(D, t_k)$ (green) . The nearest CloudSat profile to MZS (22.9 km) is also shown in black. Satellite and K2W W-band profiles showed very good agreement with each other. The difference between the K2W W-band and CloudSat was only 0.2 dB at 760 m (10.2 dBZ vs. 10.0 dBZ, respectively), 1 dB at 960 m (7.9 dBZ vs. 8.9 dBZ, respectively), and about 0.5 dB root mean square difference considering both range bins.

In Fig. 9a, the 94 GHz reflectivity profile estimated from MRR2 reflectivity data using the 35 GHz to 94 GHz reflectivity conversion formula in Maahn et al. (2014) (hereafter M14), which was argued to be applicable, at some extent, to the MRR2 wavelength, is shown for

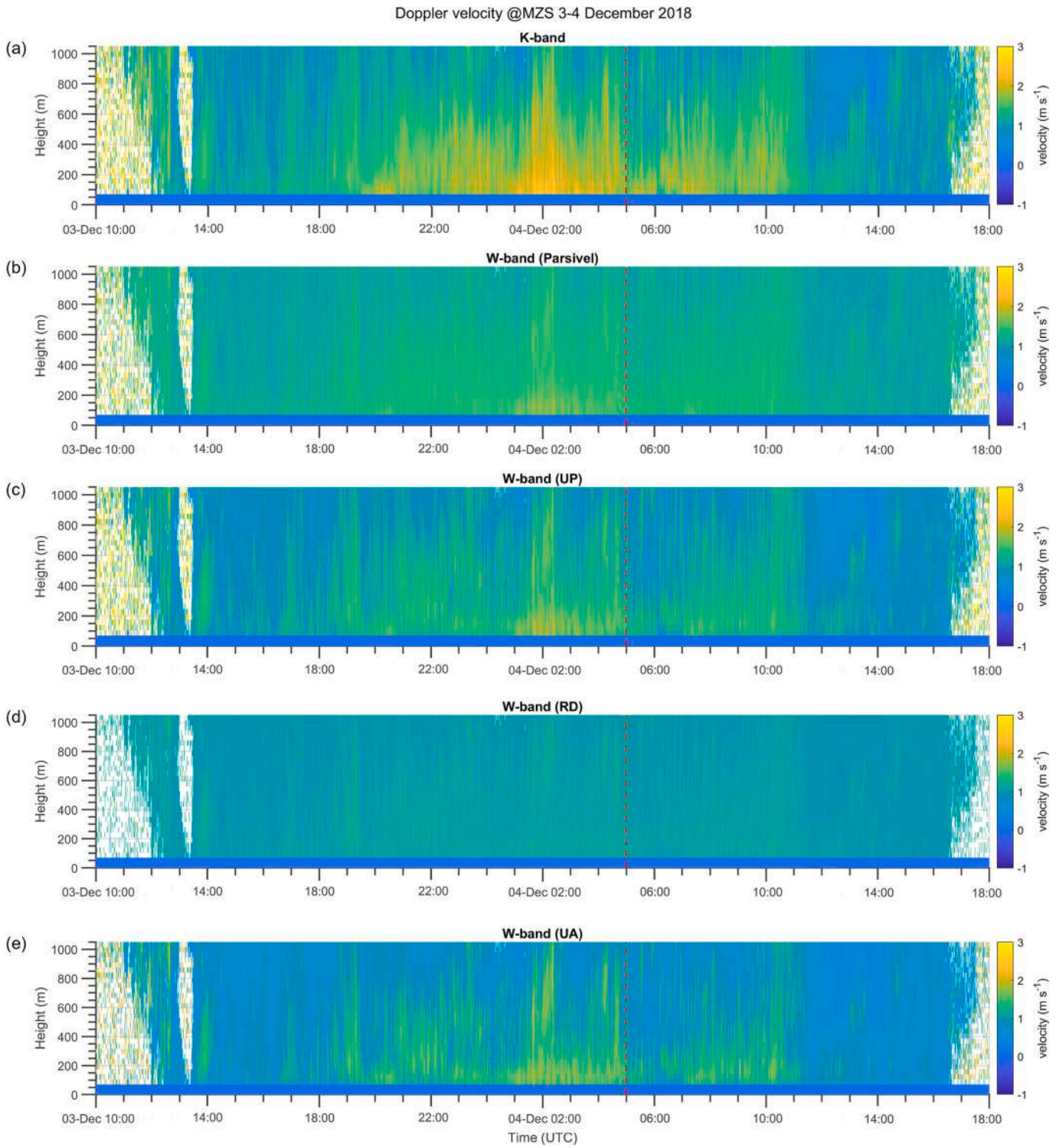

Fig. 6. Same as Fig. 5 but for Doppler velocity profiles.

comparison. It is worth mentioning that the formula proposed by Maahn et al. (2014) was derived starting from three reflectivity–snowfall rate relationships described by Kulie and Bennartz (2009) for different particle habits derived from aircraft measurements. Results showed that the K2W procedure described in this work (green line) performed better than applying the reported formula (orange line), which significantly underestimated the CloudSat profiles. For both range bins, the W-band Z_e values from M14 were considerably lower than those of CloudSat by about 5–6 dB. The specific microphysical assumptions contained in the formula of Maahn et al. (2014) could explain the large observed difference, as they probably failed to mimic the microphysical features of snowfall during the overpass. This aspect stresses the importance of having an in situ disdrometer coupled with MRR2 to investigate the snow microphysics in more detail allowing proper parameterization of the snow characteristics that are necessary for frequency conversion using K-band Doppler spectrum. The potential of the proposed methodology is further highlighted in Fig. 9b, which shows the estimated Doppler velocity profile in the W-band corresponding to Fig. 9a. The

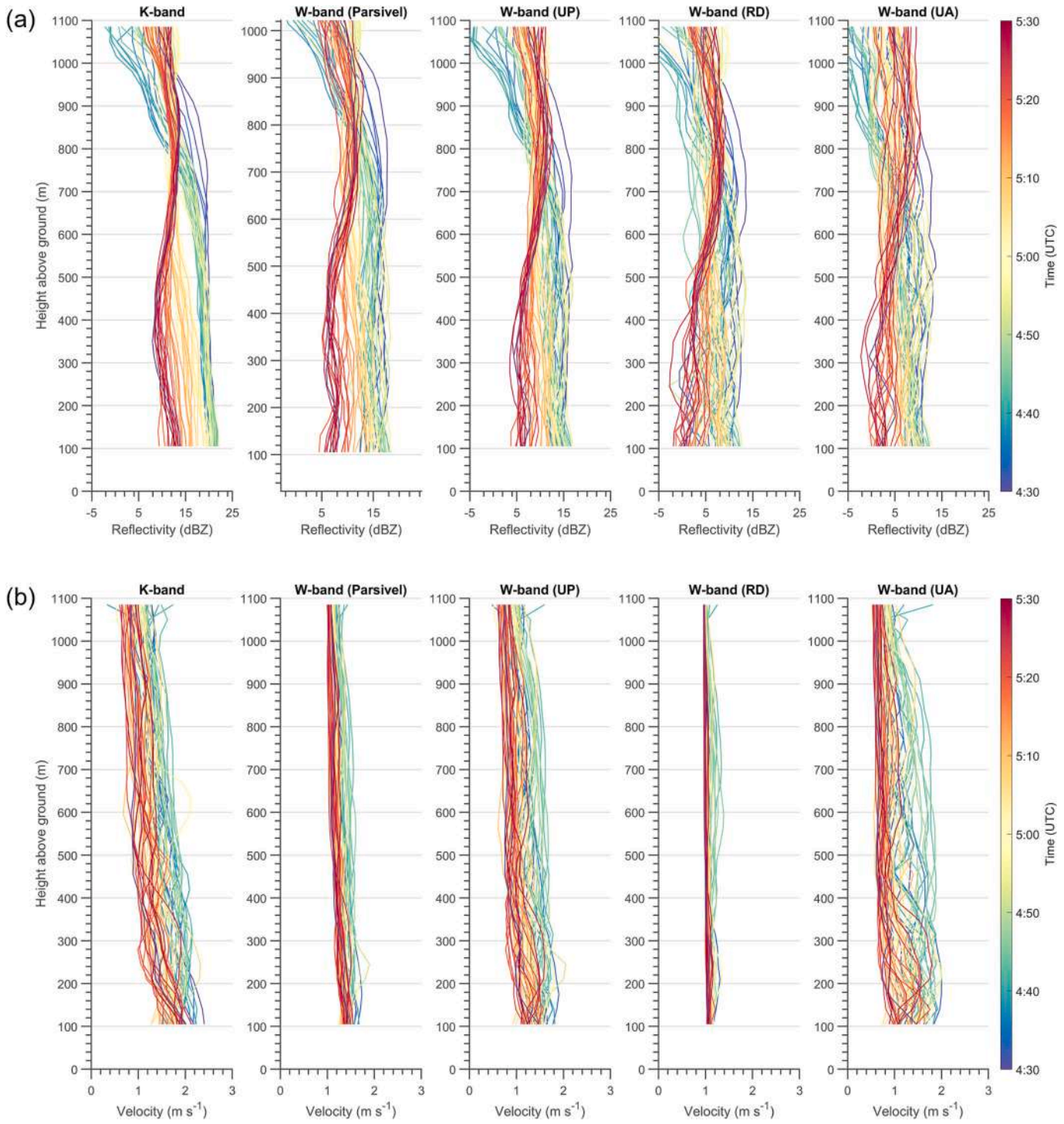

Fig. 7. Vertical profiles of (a) radar reflectivity and (b) Doppler velocity in the K-band and W-band shown in Figs. 5 and 6 but within a 1-h time window around the CloudSat overpass time. For W-band profiles, the $v_t(D)$ relationship used in the K2W is highlighted in the plot title.

standard deviation of the simulated Doppler velocity was found to be smaller than about 0.2 m s^{-1}.

The time averaging window and distance from MZS considered for Fig. 9 were further narrowed (Fig. 10a,b) or widened (Fig. 10c-e) as sensitivity analysis to take into account the spatial variability of the precipitation system during the satellite overpass. Narrowing the time resolution from 25 min, the difference between the Satellite and K2W W-band profiles became larger. The mean difference between CloudSat and K2W Z_e profiles were about 1.4 dB with 10-min time averaging (Fig. 10b), while the 1-min time window was not able to properly convert K-band reflectivity to the W-band as the two profiles were very similar (Fig. 10a). By contrast, broadening the time resolution, the K-band profile and the converted W-band profile began to become quite distinct. Further extension of the resolution windows led to a worsening of the correspondence between the reflectivities (Fig. 10c–e), also indicating a lowering of the mean CloudSat reflectivity, probably due to satellite movement away from MZS and the Antarctic coastline. It is concluded that a good agreement (< 2 dB CPR calibration error) between CloudSat profiles within 25 km from MZS and K2W can be found for 15–25 min time averaging, and the best correspondence was found

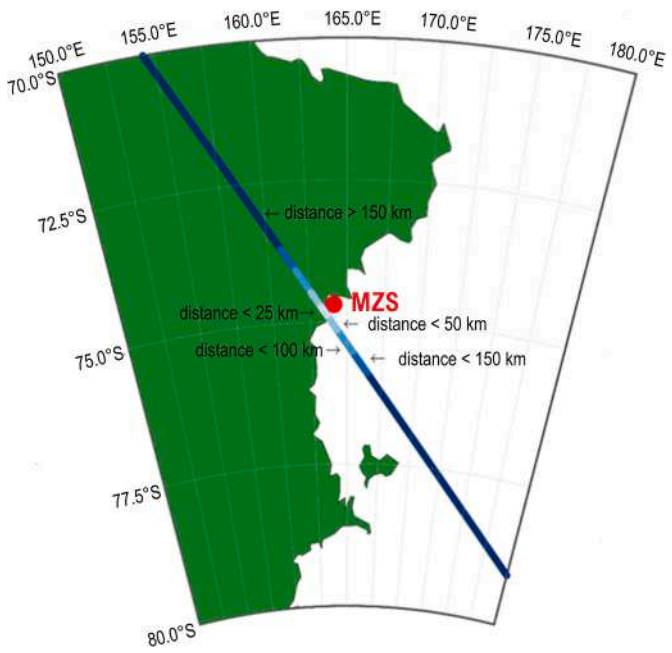

Fig. 8. Satellite track during the CloudSat overpass over MZS on 4 December 2018 around 05:00 UTC. Different colours indicate the different spatial windows, based on the distance of CloudSat profiles from MZS, which were used for sensitivity analysis reported in Fig. 10.

for 25 min time resolution. The impact of CloudSat attenuation on our results was investigated from the path integrated attenuation (PIA) product (2C-PRECIP-COLUMN, release R05), which were much smaller than 0.5 dBZ, and would not affect the conclusions drawn in this Section.

The ability to derive the 94 GHz Doppler profiles from the MRR2 K-band Doppler spectrum in addition to the radar reflectivity profiles, regardless of the satellite blind zone, could also be useful for comparing and validating measurements of satellite missions equipped with Doppler observations, such as the upcoming ESA/JAXA EarthCARE mission that will add Doppler capability to 94 GHz radar.

4. Summary

CloudSat CPR has been the major source of information about snow precipitation in Antarctica. Given the launch of the EarthCARE mission in April 2024 carrying the first W-band Doppler CPR, the development of a reliable validation strategy for the satellite measurements and retrievals is in high demand, especially in Antarctica, which suffers from extremely sparse ground measurements. A new validation methodology (K2W) was proposed to combine MRR Doppler spectra and disdrometer data to simulate 94 GHz reflectivity and Doppler measurements from satellite-borne CPR. The proposed K2W conversion methodology was assessed using CloudSat overpass data over MZS for a typical snowfall event. The main findings are as follows.

- The observed and simulated mean radar reflectivity and Doppler velocity at the K-band for snowfall in 2019–2020 Antarctic summer obtained by MRR2 and Parsivel, respectively, showed good correspondence with each other for observations close to the ground in terms of both 1:1 ratio and the time series when shorter time resolution for $\overline{v_{t,M}}(D, t_k)$ calculation was considered.
- The relationships in the literature failed to replace the $v_t(D)$ relationship derived from in situ observations and underlined the importance of the MRR2- Parsivel pairing.
- Assessment of the K2W conversion methodology with coincident CloudSat measurements concluded that the K2W methodology could reproduce the CloudSat Z_e profile with 0.2 dB mean difference at the

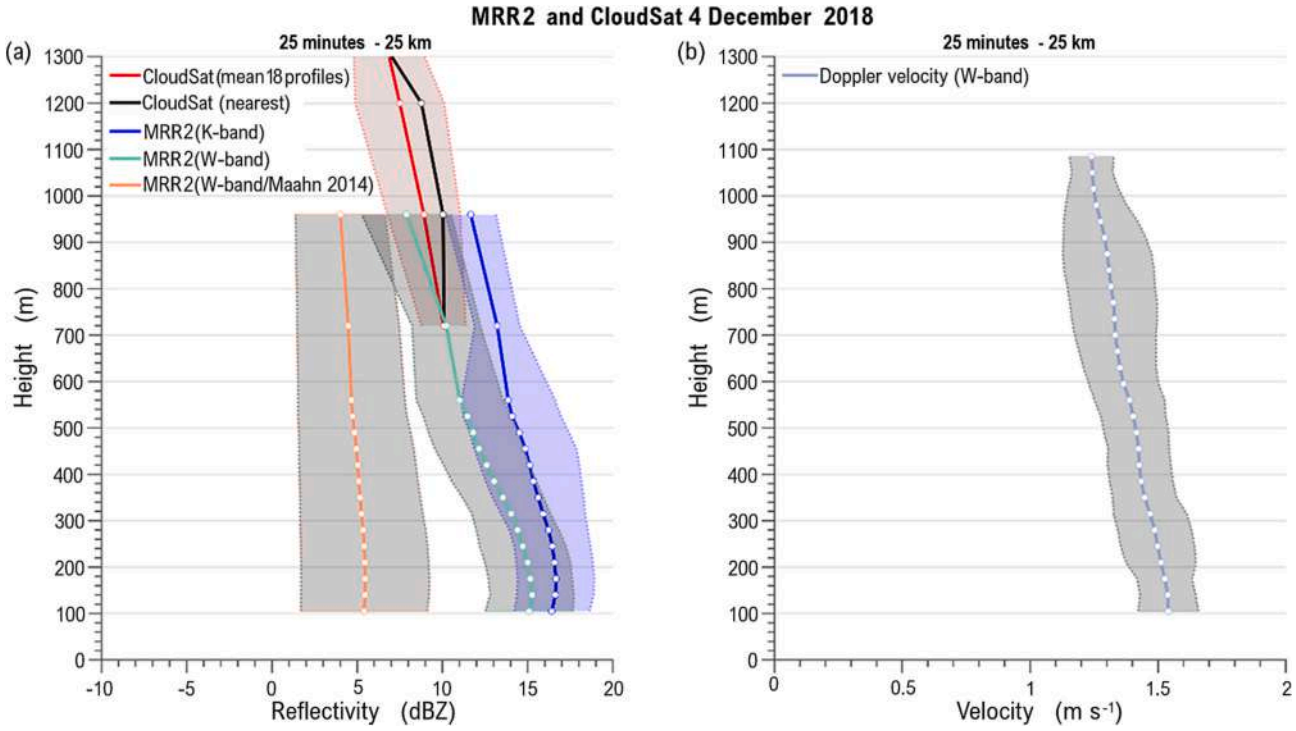

Fig. 9. (a) Comparison of CloudSat reflectivity profiles within 25 km from MZS (red) and K2W W-band $Z_{e,W}$ with 25-min time averaging (time lag of ±12.5 min) around the CloudSat overpass (green). The black, blue and the orange lines indicate the nearst CloudSat reflectivity profile, MRR2 $Z_{e,K}$ and the W-band reflectivity profile obtained according to Maahn et al. (2014), respectively. (b) The vertical Doppler velocity profile in the W-band using the K2W methodology corresponding to (a). The shaded areas represent standard deviations. (For interpretation of the references to colour in this figure legend, the reader is referred to the web version of this article.)

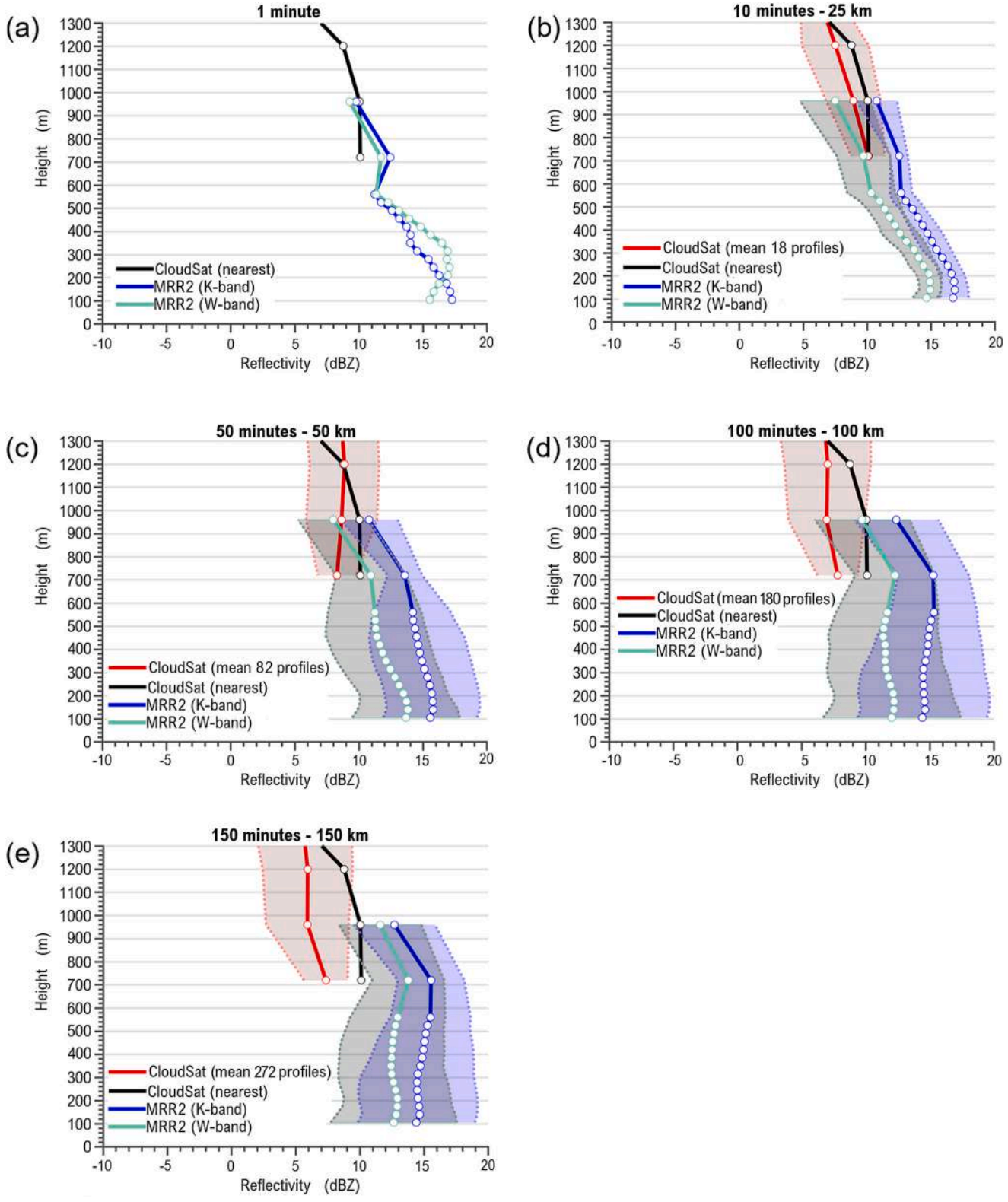

Fig. 10. Comparison of reflectivity profiles between CloudSat and K2W obtained for different spatial and time averaging. The time and spatial averaging windows specified at the top of each figure indicate the minute of Parsivel and MRR2 measurements used to calculate the mean $Z_{e,W}$ and $V_{D,W}$ profiles, and the maximum distance from MZS considered to average the CloudSat Z_e profiles, respectively. Black lines indicate the closest to MZS CloudSat profile, red lines indicate the mean vertical Z_e profiles of CloudSat (the number of profiles is presented in the legend) within the considered spatial window, blue lines indicate the mean MRR2 vertical profile in the K-band in the considered time windows around the satellite overpass, and green lines indicate the converted K2W profile. The shaded areas represent the standard deviations. (For interpretation of the references to colour in this figure legend, the reader is referred to the web version of this article.)

lowest radar range bin and 0.5 dB difference on average below 1 km altitude when a time lag of ±12.5 min around the CloudSat overpass was considered.
- The Z_e profiles within the CloudSat blind zones could be successfully simulated by the K2W methodology. The unattenuated W-band profile obtained by the K2W methodology can be used to evaluate spaceborne W-band radar retrievals.
- The W-band Doppler velocity below 1 km altitude that would be observed by EarthCARE was simulated from K-band for the first time with the K2W method. The standard deviation of the simulated Doppler velocity was found to be smaller than about 0.2 m s^{-1}.

The present study demonstrated the effectiveness of the K2W method for the simulation and validation of satellite observations employing a W-band radar. Pairs of MRR-disdrometer are available in many ground observation sites worldwide and in most of the research stations in Antarctica, therefore the K2W method has a wide application. Particularly in Antarctica, a more complete experimental set-up featuring multiwavelength radars has been installed only for a few targeted campaigns (e.g., Lubin et al., 2020). This makes the K2W method highly valuable for long-term validating satellite measurements using continuous observations provided by MRR and disdrometers over the Antarctic continent.

Latest assessment of EarthCARE CPR Doppler velocity measurement accuracy from global simulations for precipitation suggests values <0.5 m s^{-1} for $Z_e > 0$ dBZ at 10 km integration for low pulse repetition frequency (PRF) case and a smaller value for high PRF case (Hagihara et al., 2022). The K2W methodology will be used to further assess the EC-CPR Doppler velocity measurement accuracy as well as the JAXA level 2 standard products for precipitation (Sato et al., 2009; Sato and Okamoto, 2011, 2020) and their relation to ice particle habits (Okamoto et al., 2019, 2020) and mixed-phase microphysics (Sato et al., 2018, 2019) derived from EC-CPR, Atmospheric Lidar (ATLID) and Multispectral Imager (MSI).

Funding

This work is partly supported by the APP (Antarctic Precipitation Properties) project funded by the Italian National Antarctic Research Program (PNRA). K.S. was supported by The Japan Aerospace Exploration Agency [EORA3]; JSPS [KAKENHI grant JP22K03721, JP17H06139]; Shiseido Female Researcher Science Grant; Initiative for Realizing Diversity in the Research Environment; Collaborative Research Program of the Research Institute for Applied Mechanics, Kyushu University (Fukuoka, Japan).

CRediT authorship contribution statement

Alessandro Bracci: Conceptualization, Methodology, Software, Writing – original draft, Writing – review & editing, Visualization. **Kaori Sato:** Conceptualization, Methodology, Validation, Writing – review & editing, Supervision, Funding acquisition. **Luca Baldini:** Conceptualization, Methodology, Validation, Writing – original draft, Writing – review & editing, Supervision, Funding acquisition. **Federico Porcù:** Writing – review & editing, Supervision, Funding acquisition. **Hajime Okamoto:** Conceptualization, Methodology, Validation, Writing – review & editing, Supervision, Funding acquisition.

Declaration of Competing Interest

The authors declare no conflict of interest.

Data availability

Micro Rain Radar and Parsivel measurements at MZS used in this work are available upon request to L.B. (l.baldini@isac.cnr.it) and will soon be uploaded to the National Antarctic Data Center (NADC, https://iandc.pnra.aq/srv/eng/catalog.search) of Italy.

Acknowledgments

This work is also a contribution to the Year of Polar Prediction (YOPP), a flagship activity of the Polar Prediction Project (PPP), initiated by the World Weather Research Programme (WWRP) of the World Meteorological Organization (WMO). We acknowledge the WMO WWRP for its role in coordinating this international research activity. The 2C-PRECIP-COLUMN (release R05) data are obtained from the CloudSat Data Processing Center (DPC). The CloudSat-CALIPSO Merged Dataset is provided by JAXA A-Train Product Monitor. The authors also thank the Antarctic Technical Unit of ENEA and the PNRA for the logistic support to the projects at MZS and the Italian Antarctic Meteo-Climatological Observatory (https://www.climantartide.it/). Finally, this work was supported in part by the Collaborative Research Program "Analysis of ground-based and satellite observations of ice/liquid precipitation" of the Research Institute for Applied Mechanics, Kyushu University.

References

Adirosi, E., Baldini, L., Roberto, N., Gatlin, P., Tokay, A., 2016. Improvement of vertical profiles of raindrop size distribution from micro rain radar using 2D video disdrometer measurements. Atmos. Res. 169, 404–415.

Atlas, D., Srivastava, R.C., Sekhon, R.S., 1973. Doppler radar characteristics of precipitation at vertical incidence. Rev. Geophys. 11, 1. https://doi.org/10.1029/RG011i001p00001.

Battaglia, A., Rustemeier, E., Tokay, A., Blahak, U., Simmer, C., 2010. PARSIVEL snow observations: a critical assessment. J. Atmos. Ocean. Technol. 27, 333–344. https://doi.org/10.1175/2009JTECHA1332.1.

Bracci, A., Baldini, L., Roberto, N., Adirosi, E., Montopoli, M., Scarchilli, C., Grigioni, P., Ciardini, V., Levizzani, V., Porcù, F., 2022. Evidence of sublimation in the vertical profiles of radar reflectivity and its impact on snowfall estimation at the ground at Mario Zucchelli Antarctic Station. In: 2022 3rd URSI Atlantic and Asia Pacific Radio Science Meeting (AT-AP-RASC). IEEE. https://doi.org/10.23919/AT-AP-RASC54737.2022.9814266.

Bracci, A., Baldini, L., Roberto, N., Adirosi, E., Montopoli, M., Scarchilli, C., Grigioni, P., Ciardini, V., Levizzani, V., Porcù, F., 2021. Quantitative precipitation estimation over Antarctica using different ze-SR relationships based on snowfall classification combining ground observations. Remote Sens. 14, 82. https://doi.org/10.3390/rs14010082.

Bringi, V.N., Chandrasekar, V., 2001. Polarimetric doppler weather radar: principles and applications. Cambridge University Press.

Capozzi, V., Montopoli, M., Bracci, A., Adirosi, E., Baldini, L., Vulpiani, G., Budillon, G., 2020. Retrieval of snow precipitation rate from polarimetric X-band radar measurements in southern Italy apennine mountains. Atmos. Res. 236, 104796 https://doi.org/10.1016/j.atmosres.2019.104796.

Chen, B., Wang, J., Gong, D., 2016. Raindrop size distribution in a midlatitude continental squall line measured by Thies optical disdrometers over East China. J. Appl. Meteorol. Climatol. 55, 621–634. https://doi.org/10.1175/JAMC-D-15-0127.1.

Draine, B.T., 1988. The discrete-dipole approximation and its application to interstellar graphite grains. Astrophys. J. 333, 848–872.

Draine, B.T., Flatau, P.J., 1994. Discrete-dipole approximation for scattering calculations. J. Opt. Soc. Am. A. 11, 1491–1499.

Foote, G.B., Du Toit, P.S., 1969. Terminal velocity of raindrops aloft. J. Appl. Meteor. Climatol. 8, 249–253.

Frezzotti, M., Scarchilli, C., Becagli, S., Proposito, M., Urbini, S., 2013. A synthesis of the Antarctic surface mass balance during the last 800 yr. Cryosph. 7, 303–319.

Gorgucci, E., Baldini, L., 2015. Influence of beam broadening on the accuracy of radar polarimetric rainfall estimation. J. Hydrometeorol. 16, 1356–1371. https://doi.org/10.1175/JHM-D-14-0084.1.

Grazioli, J., Genthon, C., Boudevillain, B., Duran-Alarcon, C., Del Guasta, M., Madeleine, J.B., Berne, A., 2017a. Measurements of precipitation in Dumont d'Urville, Adélie land, East Antarctica. Cryosphere 11, 1797–1811. https://doi.org/10.5194/tc-11-1797-2017.

Grazioli, J., Madeleine, J.-B., Gallée, H., Forbes, R.M., Genthon, C., Krinner, G., Berne, A., 2017b. Katabatic winds diminish precipitation contribution to the Antarctic ice mass balance. Proc. Natl. Acad. Sci. 114, 10858–10863. https://doi.org/10.1073/pnas.1707633114.

Hagihara, Y., Ohno, Y., Horie, H., Roh, W., Satoh, M., Kubota, T., Oki, R., 2022. Assessments of doppler velocity errors of EarthCARE cloud profiling radar using global cloud system resolving simulations: effects of doppler broadening and folding. IEEE Trans. Geosci. Remote Sens. 60, 1–9. https://doi.org/10.1109/TGRS.2021.3060828.

Hagihara, Y., Okamoto, H., Yoshida, R., 2010. Development of a combined CloudSat-CALIPSO cloud mask to show global cloud distribution. J. Geophys. Res. Atmos. 115, 1–17. https://doi.org/10.1029/2009JD012344.

Illingworth, A., Barker, H., Chepfer, H., Delanoe, J., Domenech, C., Donovan, D., Hogan, R., Huenerbein, A., Kollias, P., Nakajima, T., Nakajima, T., Nishizawa, T., Ohno, Y., Okamoto, H., Sato, K., Satoh, M., Wandinger, U., Wehr, T., Zadelhoff, G., 2015. The EarthCare satellite: the next step forward in global measurements of clouds, aerosols, precipitation and radiation. Bull. Amer. Meteor. Soc. 96, 1311–1332.

IPCC, 2021. Climate change 2021: The physical science basis. In: Contribution of Working Group I to the Sixth Assessment Report of the Intergovernmental Panel on Climate Change. Geneva, Switzerland.

Kulie, M.S., Bennartz, R., 2009. Utilizing spaceborne radars to retrieve dry snowfall. J. Appl. Meteorol. Climatol. 48, 2564–2580. https://doi.org/10.1175/2009JAMC2193.1.

Kuo, K.Sen, Olson, W.S., Johnson, B.T., Grecu, M., Tian, L., Clune, T.L., Van Aartsen, B. H., Heymsfield, A.J., Liao, L., Meneghini, R., 2016. Full access the microwave radiative properties of falling snow derived from nonspherical ice particle models. Part I: an extensive database of simulated pristine crystals and aggregate particles, and their scattering properties. J. Appl. Meteorol. Climatol. 55, 691–708. https://doi.org/10.1175/JAMC-D-15-0130.1.

Li, H., Moisseev, D., 2020. Two layers of melting ice particles within a single radar bright band: interpretation and implications. Geophys. Res. Lett. 47, 1–10. https://doi.org/10.1029/2020GL087499.

Liao, L., Meneghini, R., Tian, L., Heymsfield, G.M., 2008. Retrieval of snow and rain from combined X- and W-band airborne radar measurements. IEEE Trans. Geosci. Remote Sens. 46, 1514–1524. https://doi.org/10.1109/TGRS.2008.916079.

Locatelli, J.D., Hobbs, P.V., 1974. Fall speeds and masses of solid precipitation particles. J. Geophys. Res. 79, 2185–2197. https://doi.org/10.1029/JC079i015p02185.

Lubin, D., Zhang, D., Silber, I., Scott, R.C., Kalogeras, P., Battaglia, A., Vogelmann, A.M., 2020. AWARE: the atmospheric radiation measurement (ARM) West Antarctic radiation experiment. Bull. Am. Meteorol. Soc. 101 (7), E1069–E1091. https://doi.org/10.1175/BAMS-D-18-0278.1.

Maahn, M., Burgard, C., Crewell, S., Gorodetskaya, I.V., Kneifel, S., Lhermitte, S., Van Tricht, K., van Lipzig, N.P.M., 2014. How does the spaceborne radar blind zone affect derived surface snowfall statistics in polar regions? J. Geophys. Res. 119, 13604–13620. https://doi.org/10.1002/2014JD022079.

Maahn, M., Kollias, P., 2012. Improved micro rain radar snow measurements using doppler spectra post-processing. Atmos. Meas. Tech. 5, 2661–2673. https://doi.org/10.5194/amt-5-2661-2012.

Marchand, R., Mace, G., 2018. Level 2 GEOPROF Product Process Description and Interface Control Document.. URL: https://www.cloudsat.cira.colostate.edu/clouds at-static/info/dl/2b-geoprof/2B-GEOPROF_PDICD.P1_R05.rev0_0.pdf.

Marchand, R., Mace, G.G., Ackerman, T., Stephens, G., 2008. Hydrometeor detection using CloudSat—An earth-orbiting 94-GHz cloud radar. J. Atmos. Ocean. Technol. 25, 519–533.

Matrosov, S.Y., 2021. Polarimetric radar variables in snowfall at ka-and W-band frequency bands: a comparative analysis. J. Atmos. Ocean. Technol. 38, 91–101. https://doi.org/10.1175/JTECH-D-20-0138.1.

Matrosov, S.Y., 2019. Comparative evaluation of snowfall retrievals from the CloudSat W-band radar using ground-based weather radars. J. Atmos. Ocean. Technol. 36, 101–111. https://doi.org/10.1175/JTECH-D-18-0069.1.

Medley, B., Thomas, E.R., 2019. Increased snowfall over the Antarctic ice sheet mitigated twentieth-century sea-level rise. Nat. Clim. Chang. 9, 34–39. https://doi.org/10.1038/s41558-018-0356-x.

METEK, 2015. MRR Physical Basics, Metek.

Molthan, A.L., Colle, B.A., Yuter, S.E., Stark, D., 2016. Comparisons of modeled and observed reflectivities and fall speeds for snowfall of varied riming degrees during winter storms on long Island, New York. Mon. Weather Rev. 144, 4327–4347. https://doi.org/10.1175/MWR-D-15-0397.1.

Okamoto, H., Sato, K., Borovoi, A., Ishimoto, H., Masuda, K., Konoshonkin, A., Kustova, N., 2020. Wavelength dependence of ice cloud backscatter properties for space-borne polarization lidar applications. Opt. Express 28 (20), 29178–29191. https://doi.org/10.1364/OE.400510.

Okamoto, H., Sato, K., Borovoi, A., Ishimoto, H., Masuda, K., Konoshonkin, A., Kustova, N., 2019. Interpretation of lidar ratio and depolarization ratio of ice clouds using spaceborne high-spectral-resolution polarization lidar. Opt. Express 27 (25), 36587–36600. https://doi.org/10.1364/OE.27.036587.

Okamoto, H., Nishizawa, T., Takemura, T., Sato, K., Kumagai, H., Ohno, Y., Sugimoto, N., Shimizu, A., Matsui, I., Nakajima, T., 2008. Vertical cloud properties in the tropical western Pacific Ocean: validation of the CCSR/NIES/FRCGC GCM by shipborne radar and lidar. J. Geophys. Res. Atmos. 113, 1–17. https://doi.org/10.1029/2008JD009812.

Okamoto, H., Nishizawa, T., Takemura, T., Kumagai, H., Kuroiwa, H., Sugimoto, N., Matsui, I., Shimizu, A., Emori, S., Kamei, A., Nakajima, T., 2007. Vertical cloud structure observed from shipborne radar and lidar: midlatitude case study during the MR01/K02 cruise of the research vessel mirai. J. Geophys. Res. Atmos. 112, 1–22. https://doi.org/10.1029/2006JD007628.

Okamoto, H., 2002. Information content of the 95 GHz cloud radar signals: theoretical assessment of effects of non-sphericity and error evaluations of the discrete dipole approximation. J. Geophys. Res. 107 (D22), 4628. https://doi.org/10.1029/2001JD001386.

Okamoto, H., Macke, A., Quante, M., Raschke, E., 1995. Modeling of back- scattering by non-spherical ice particles for the interpretation of cloud radar signals at 94GHZ. An error analysis. Contrib. Atmos. Phys. 68, 319–334.

Peters, G., Fischer, B., Andersson, T., 2002. Rain observations with a vertically looking micro rain radar (MRR). Boreal Environ. Res. 7, 353–362.

Protat, A., Bouniol, D., Delanoë, J., May, P.T., Plana-Fattori, A., Hasson, A., O'Connor, E., Görsdore, U., Heymsfield, A.J., 2009. Assessment of Cloudsat reflectivity measurements and ice cloud properties using ground-based and airborne cloud radar observations. J. Atmos. Ocean. Technol. 26, 1717–1741. https://doi.org/10.1175/2009JTECHA1246.1.

Sato, K., Okamoto, H., 2020. Application of single and multiple-scattering theories to analyses of spaceborne cloud radar and lidar data. In: Kokhanovsky, A. (Ed.), Springer Series in Light Scattering, vol. 5. Springer Nature, pp. 1–37. https://doi.org/10.1007/978-3-030-38696-2.

Sato, K., Okamoto, H., Ishimoto, H., 2019. Modeling the depolarization of space-borne lidar signals. Opt. Express 27 (4), A117–A132. https://doi.org/10.1364/OE.27.00A117.

Sato, K., Okamoto, H., Ishimoto, H., 2018. Physical model for multiple scattered space-borne lidar returns from clouds. Opt. Express 26 (6), A301–A319. https://doi.org/10.1364/OE.26.00A301.

Sato, K., Okamoto, H., 2011. Refinement of global ice microphysics using spaceborne active sensors. J. Geophys. Res. Atmos. 116, D20202. https://doi.org/10.1029/2011JD01588.

Sato, K., Okamoto, H., Yamamoto, M.K., Fukao, S., Kumagai, H., Ohno, Y., Horie, H., Abo, M., 2009. 95-GHz doppler radar and lidar synergy for simultaneous ice microphysics and in-cloud vertical air motion retrieval. J. Geophys. Res. Atmos. 114, D03203. https://doi.org/10.1029/2008JD010222.

Scarchilli, C., Ciardini, V., Grigioni, P., Iaccarino, A., De Silvestri, L., Baldini, L., Roberto, N., Argentini, S., Bracci, A., Frezzotti, M., 2020. Characterization of snowfall estimated by in situ and ground-based remote-sensing observations at Terra Nova Bay, Victoria Land, Antarctica. J. Glaciol. 66, 1006–1023. https://doi.org/10.1017/jog.2020.70.

Schoger, S.Y., Moisseev, D., von Lerber, A., Crewell, S., Ebell, K., 2021. Snowfall-Rate Retrieval for K- and W-Band Radar Measurements Designed in Hyytiälä, Finland, and Tested at Ny-Ålesund, Svalbard, Norway. J. Appl. Meteorol. Climatol. 60, 273–289. https://doi.org/10.1175/JAMC-D-20-0095.1.

Souverijns, N., Gossart, A., Lhermitte, S., Gorodetskaya, I.V., Kneifel, S., Maahn, M., Bliven, F.L., van Lipzig, N.P.M., 2017. Estimating radar reflectivity - snowfall rate relationships and their uncertainties over Antarctica by combining disdrometer and radar observations. Atmos. Res. 196, 211–223. https://doi.org/10.1016/j.atmosres.2017.06.001.

Stephens, G., Winker, D., Pelon, J., Trepte, C., Vane, D., Yuhas, C., L'Ecuyer, T., Lebsock, M., 2018. Cloudsat and CALIPSO within the a-train: ten years of actively observing the earth system. Bull. Am. Meteorol. Soc. 99, 569–581. https://doi.org/10.1175/BAMS-D-16-0324.1.

Tanelli, S., Durden, S.L., Im, E., Pak, K.S., Reinke, D.G., Partain, P., Haynes, J.M., Marchand, R.T., 2008. CloudSat's cloud profiling radar after two years in orbit: performance, calibration, and processing. IEEE Trans. Geosci. Remote Sens. 46, 3560–3573. https://doi.org/10.1109/TGRS.2008.2002030.

von Lerber, A., Moisseev, D., Bliven, L.F., Petersen, W., Harri, A.M., Chandrasekar, V., 2017. Microphysical properties of snow and their link to ze-S relations during BAECC 2014. J. Appl. Meteorol. Climatol. 56, 1561–1582. https://doi.org/10.1175/JAMC-D-16-0379.1.